Wind-induced vibration control of base-isolated high-rise buildings by using tuned mass damper inerter

Huergo, Iván F.; Hernández-Barrios, Hugo; Morales-Nápoles, Oswaldo

DOI
10.1080/15732479.2025.2527914

Publication date
2025

Document Version
Final published version

Published in
Structure and Infrastructure Engineering

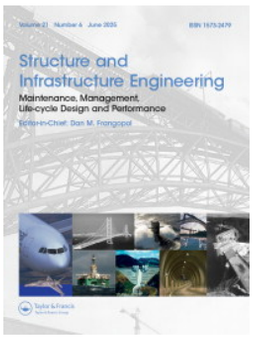

Taylor & Francis
Taylor & Francis Group

Structure and Infrastructure Engineering
Maintenance, Management, Life-Cycle Design and Performance

ISSN: 1573-2479 (Print) 1744-8980 (Online) Journal homepage: www.tandfonline.com/journals/nsie20

Wind-induced vibration control of base-isolated high-rise buildings by using tuned mass damper inerter

Iván F. Huergo, Hugo Hernández-Barrios & Oswaldo Morales-Nápoles

To cite this article: Iván F. Huergo, Hugo Hernández-Barrios & Oswaldo Morales-Nápoles (06 Jul 2025): Wind-induced vibration control of base-isolated high-rise buildings by using tuned mass damper inerter, Structure and Infrastructure Engineering, DOI: 10.1080/15732479.2025.2527914

To link to this article: https://doi.org/10.1080/15732479.2025.2527914

STRUCTURE AND INFRASTRUCTURE ENGINEERING
https://doi.org/10.1080/15732479.2025.2527914

Wind-induced vibration control of base-isolated high-rise buildings by using tuned mass damper inerter

Iván F. Huergo[a], Hugo Hernández-Barrios[b] and Oswaldo Morales-Nápoles[c]

[a]School of Engineering and Technologies, Universidad de Monterrey, San Pedro Garza García, Mexico; [b]School of Engineering, Universidad Michoacana de San Nicolás de Hidalgo, Morelia, Mexico; [c]Faculty of Civil Engineering and Geosciences, Delft University of Technology, The Netherlands

ABSTRACT

Base isolation of high-rise buildings has growing popularity to limit peak floor accelerations under seismic loads; however, it may increase susceptibility to wind-induced vibrations due to the increase in fundamental vibration period. This study presents an equivalent coupled-two-beam (CTB) model incorporating base isolation (BI) and a tuned mass damper inerter (TMDI) to evaluate passive vibration control under lateral wind loads for various lateral resisting systems. A 144-meter-tall building was analyzed under along-wind and across-wind loads simulated as Gaussian processes, considering six isolator-damper configurations: (1) fixed-base (FB), (2) FB with a top TMDI (FB-TTMDI), (3) BI, (4) BI with a top TMDI (BI-TTMDI), (5) BI with a bottom TMDI (BI-BTMDI), and (6) BI with double TMDI (BI-DTMDI). TMDIs were compared to traditional tuned mass dampers (TMDs) to assess mass amplification under varying base isolator damping. Optimization strategies were explored to enhance vibration control: for FB-TTMDI, the TMDI placement minimized RMS accelerations, while for BI-TTMDI, it was optimized to reduce peak displacement. Finally, design guidelines are provided for ultimate and serviceability limit states. Results indicate hybrid control systems are most effective when lateral deformation resembles pure bending, making them suited for shear wall-frame and tubular systems.

ARTICLE HISTORY
Received 11 October 2024
Revised 7 February 2025
Accepted 18 March 2025

KEYWORDS
Base isolation; high-rise buildings; lateral resisting systems; tuned mass damper inerter; vibration control optimization; wind-induced vibrations; wind load simulation

1. Introduction

Base isolation has become an effective design strategy to mitigate seismic hazard of low-rise buildings, that is, rigid structures with a small fundamental period of vibration. The principle of base isolation is based on the decoupling of the superstructure from the earthquake ground motion by introducing a flexible interface between the foundation and the base of the structure. Thereby, the isolation system shifts the fundamental time period of the structure to a large value avoiding the resonance phenomenon with the time period of ground motion, which results in great reductions of inter-story drifts and floor accelerations.

According to Saha et al. (2015), the most commonly used base isolation systems (BIS) in practical applications are the following ones: (1) laminated rubber bearings (LRBs), (2) lead-rubber bearings (New Zealand, N-Z system), (3) friction pendulum systems (FPSs) and (4) resilient-friction base isolators (RFBIs). LRBs consist of alternate layers of rubber and metal plates and can be divided into two categories: low damping rubber bearings (LDRBs) and high damping rubber bearings (HDRBs). A lead-rubber bearing (N-Z system) is similar to the LRB with additional central lead-core provided as a means of additional energy dissipation (Jangid & Data, 1995), which also provides initial rigidity against wind loads and minor earthquakes. On the other hand, the restoring force in a FPS is generated due to the raising of the structure caused by the concave geometry of the isolator, that is, the response of a FPS depends on the friction coefficient and the geometry of the system (Zayas et al., 1990). Finally, sliding flat ring elements and central rubber core are constituents of RFBIs and the sliding rings are Teflon-coated to reduce friction while flexible cover is used as protection against corrosion and dust (Mostaghel & Khodaverdian, 1987).

According to Naeim and Kelly (1999), the ratio between the fundamental period of the base isolation system, T_{BIS}, and the fundamental period of the superstructure, T_1, must be greater than or equal to 3, that is, $T_{BIS}/T_1 \geq 3$. Based on the linear theory, the fundamental mode of vibration of an isolated structure is closely related to the degree of freedom assigned to the lateral displacement of the isolation system. In this way, the higher modes of vibration contribute to the lateral deformation and movement of the superstructure, which results in damage of the structural system, nonstructural system and contents of the isolated structure (Naeim & Kelly, 1999). Saiful et al. (2011) detailed the major steps that should be followed to assess a structure whether it is suitable for base isolation or not. For seismic design purposes, rigid structures, that is, short period structures, are usually the most likely to be isolated because the aim is to

CONTACT Iván F. Huergo ivan.huergo@udem.edu School of Engineering and Technologies, Universidad de Monterrey, San Pedro Garza García, Mexico.
Supplemental data for this article can be accessed online at https://doi.org/10.1080/15732479.2025.2527914.

avoid the resonant response on hard rock or soils with a short period of vibration.

Slender structures usually have overturning problems when gravity and lateral loads are applied simultaneously, which can cause tensile stresses in the base isolators. Most practical isolation devices have been manufactured to resist compression loads, however, there are alternatives to avoid the transfer of tensile stresses to the base isolators, e.g. the tensile stresses in the base isolators of the Ñuñoa Capital Building in Chile were avoided by connecting the slabs of the two towers on the lower 4 stories and by using a 2 m thick slab resting directly on the isolators (Lagos et al., 2014).

In recent years, base isolation of medium and high-rise buildings has growing popularity to limit peak floor accelerations under seismic loads, which is useful for design of building contents. To-date, just under 200 isolated high-rise buildings, ranging from 60 to 180 meters tall, have been constructed in Japan, with the most common implementation being for concrete residential condominium buildings (Becker et al., 2015). Accordingly, Table 1 shows some real examples of mid-rise and high-rise buildings with seismic isolation (Boardman et al., 1983; Elsesser et al., 1995; Komuro et al., 2005; Lagos et al., 2014; Nakagawa et al., 2015; Youssef et al., 2000).

For base-isolated shear buildings under earthquakes loads, Matsagar and Jangid (2004) determined that the flexibility of superstructure increases the superstructure acceleration, however, the bearing displacements were not much influenced by the superstructure flexibility. Accordingly, the mitigation of floor accelerations induced by earthquakes is crucial to avoid damage of contents, however, an increment of base isolation damping does not contribute to reduce floor accelerations because contents usually have small periods of vibration (Zúñiga-Cuevas & Terán-Gilmore, 2012). Although increasing the level of damping in the isolation system tends to increase the contribution of higher modes, the use of structural systems where $8 \leq T_{BIS}/T_1 \leq 10$ results in adequate control of the contribution of higher modes (Zúñiga-Cuevas & Terán-Gilmore, 2012). According to Zúñiga-Cuevas and Terán-Gilmore (2012, 2013), a structural damping ratio less than or equal to 0.1 in combination with values of $T_{BIS}/T_1 \geq 6$ may be effective in controlling earthquake-induced floor accelerations, however, flexible structures may become more susceptible to wind-induced vibrations.

Wind loads cannot give rise to considerable loses to isolated buildings whose design strength is based on its anti-seismic capability, but the habitability problem will be caused because wind loadings can induce excessive acceleration. According to Liang et al. (2002), the damping ratio of the base isolation system (BIS) can effectively suppress the acceleration wind-induced response of the superstructure and the isolation system, but it gives little effects on the displacement of the isolation system. In a similar way, Saha et al. (2015) concluded that an increase in the isolation period of vibration increases the top floor wind-induced acceleration and bearing displacement for different kind of BIS (laminated rubber bearing, lead-rubber bearings, friction pendulum system and resilient friction bearing isolator), however, an increase in the damping of the elastomeric systems showed beneficial effect to reduce the top floor wind-induced acceleration. Based on a practical project in software ETABS, Wu et al. (2016) determined that the design value of horizontal bearing capacity of lead rubber bearing appropriate to be close to the seismic isolation layer under wind load excitation.

Based on a pure shear model, Li et al. (2020) studied the along-wind dynamic response of a base-isolated tall building by using equivalent static wind loads of both Chinese and Japanese codes. In this study, they concluded that the along-wind responses of the base-isolated building increase compared to the fixed-base building, however, the Chinese code overestimates the maximum acceleration compared to the Japanese code. Furthermore, the results showed that an increase of base-isolation stiffness is very effective to reduce the top displacement, on the other hand, an increase of base-isolation damping leads to a reduction of the top-floor acceleration induced by along-wind loads. Under strong wind excitations, the BIS of a high-rise building could yield when the wind flow is perpendicular to the windward side, however, significant inelastic displacements of the BIS could also occur when the wind direction changes (Pang et al., 2022).

For slender buildings with aspect ratios over 3, the across-wind vibration is usually greater than the along-wind vibration, on the other hand, the wind-induced torsional vibration becomes critical not only for asymmetric buildings with lateral-torsional coupling but also for rectangular buildings with wider side faces (Huergo et al., 2022). For base-isolated high-rise buildings, Tian and Chen (2023) determined that eccentricities of mass and resistance amplify the along-wind response but has relatively less influence on the larger crosswind and torsional responses, on the other hand, the base isolation with inelastic response is more effective for buildings with eccentricity as compared to buildings without eccentricity. In a similar way, Li et al.

Table 1. Real cases of base-isolated mid-rise and high-rise buildings.

Building	Location	Height [m]	Lateral resisting system
Union House	New Zealand	45	Braced frame
ÑuÑoa Capital	Santiago	75	Framed tube
Sendai MT Building	Sendai	84.9	Moment-resisting frame
City Hall	Oakland	99	Braced frame
Shimizu Corporation Headquarters	Tokyo	106	Framed tube-in-tube
Shinagawa Season Terrace	Tokyo	131	Framed tube
Thousand Tower	Kawasaki	135	Moment-resisting frame
City Hall	Los Angeles	140	Shear wall-frame system
Tokyo Skytree East Tower	Tokyo	158	Framed tube
Nakanoshima Festival Tower	Osaka	200	Megatruss/belt truss/prime columns

(2023) studied the effect of multiple FPSs to control the coupled dynamic response of base-isolated high-rise buildings under synchronous three-dimensional (3D) wind loads.

Base isolation can significantly reduce the dynamic response of the superstructure, however, the low lateral stiffness of BIS may potentially cause unacceptable large lateral displacements which must be reduced by some energy dissipation mechanism such as tuned mass dampers (TMDs). In this way, tuned mass dampers (TMDs) are devices attached to structures in order to reduce mechanical vibrations, consisting of a mass mounted on damped springs. TMDs are tuned to the fundamental period of vibration of the building to vibrate in resonance instead of the primary structure. A single TMD tuned to the fundamental mode of vibration is adequate for reducing the seismic response of base-isolated buildings because it acts as a rigid body motion that dominates the resulting vibration. According to Tsai (1995), the response reduction by the TMD becomes more prominent if the isolation system has less damping because the device can add damping to the structure during the subsequent response to the first few seconds of earthquake excitation. Unlike the typical applications to fixed-base buildings in which the TMD is placed in an upper floor or at the roof where large accelerations occur, in base-isolated shear structures subjected to seismic loads, the maximum relative displacements are concentrated at the isolation level, which justifies the implementation of the TMD above or below the isolation floor (Tsai, 1995).

Providing supplemental damping reduces the large displacements in the BIS, but at the expense of increasing interstory drifts and floor accelerations for the superstructure (Kelly, 1999). An alternative effective strategy is to attach a tuned mass damper (TMD) immediately above or below the isolation floor (Taniguchi et al., 2008; Tsai, 1995; Xiang & Nishitani, 2014; Yang et al., 1991). In order to enhance the effectiveness of the TMD without simultaneously amplifying the relevant mass ratio, the use of the inerter (Smith, 2002) has been recently proposed in conjunction with the TMD. In this way, the resulting passive control device is called a tuned mass damper inerter (TMDI). According to De Domenico and Ricciardi (2018), the inerter in the TMDI is a mechanical device that ideally produces a force proportional to the relative acceleration between its two terminals, providing rotational inertia to the system. The physical mass amplification effect is achieved by using a J damper (inertance), which is an inertial damper commonly used in Formula 1 cars. According to De Domenico and Ricciardi (2018), a TMDI reduces its performance sensitivity to the tuning frequency and to the earthquake frequency content, which makes the TMDI particularly suitable for nonlinear base-isolated structures because the stiffness of base isolators can change depending of the magnitude of ground motion.

As already mentioned before, the use of base isolators increases the flexibility of the superstructure, which can make it more susceptible to wind loads. However, TMDs are ideal devices to reduce structural motion due to wind because of the highly periodic nature of wind loads (Steyer, 2002). For along-wind loads, Kareem (1997) determined that both the lower and top TMDs aid in mitigating wind induced response of base-isolated buildings, however, the lower TMD is significantly more effective. For fixed-base flexible buildings under along-wind loads, Dai et al. (2019) determined that the control performance of tuned mass damper inerters (TMDIs) is superior to that of the conventional TMD if the end of inerter is located in the position with a relatively small controlled mode value, which depends on the mass an inertance of the TMDI. For the case of fixed-base tall buildings under across-wind loads, Giaralis and Petrini (2017) found that the TMDI reduces peak top-floor acceleration more effectively than a same weight TMD by meeting two conditions: (1) smaller attached-mass values and (2) TMDI topologies in which the inerter spans more stories in linking the attached mass to the host structure. In a similar way, Petrini et al. (2020) found that optimally tuned TMDIs become more robust than TMDs for same secondary mass as long as inertance above a certain limiting value is provided. This value depends on the secondary mass and on the number of floors spanned by the inerter: the lower the secondary mass and/or the more floors are spanned by the inerter, the lower the critical inertance value is.

The lateral resisting systems usually used for low-rise buildings are moment-resisting frames and braced frames, however, it usually changes as the height of the building increases because the aim is to reduce in a more effective way the lateral response of building when it is subjected to seismic or wind loads. According to Jayachandran (2009), the most commonly used lateral resisting systems for medium and high-rise buildings are moment-resisting frames, shear wall-frame systems, shear truss-outrigger braced systems, framed-tubes, tube-in-tube systems with interior columns, bundled tubes, truss tubes without interior columns and modular tubes. The lateral deformation of buildings strongly depends on the type of lateral resisting system, which is usually depends on the height of the building. Accordingly, low-rise buildings typically behave as shear beams; however, the lateral deformation of medium-rise and high-rise buildings sometimes resembles that of a beam in pure bending, while in other cases it results from a combination of bending and shear. Regarding the use of TMDIs, there are recent studies (Das et al., 2024; Quan et al., 2023; Su et al., 2022) that focus on the control of wind-induced response in slender structures, however, they usually consider pure shear deformations for high-rise buildings and pure bending deformations for slender chimneys. This reflects the urgent need to develop a simplified model that incorporates the effect of different lateral resisting systems when evaluating the effectiveness of TMDIs in controlling wind-induced response.

As already mentioned above, base isolation of medium and high-rise buildings has growing popularity to limit peak floor accelerations under seismic loads, however, the structure may become more susceptible to wind-induced vibrations due to not only the base isolation system (BIS) but also the lateral resisting system. Unfortunately, previous studies related to base isolation, seismic loads, wind loads, TMDs and TMDIs do not contemplate the effect of the

lateral resisting system on the dynamic response of the building. Therefore, the contribution of this paper is the proposal of a simplified mathematical model to control the undesirable effects of wind on base-isolated high-rise buildings with different lateral resisting systems by using TMDIs. Furthermore, the model is used to assess the effect of the mass ratio, damping ratio and optimization of TMDIs not only for ultimate and serviceability limit states, but also for contents design.

2. Base-isolated coupled-two-beam model with TMDI

Based on Figure 1, the non-linear hysteretic restoring force of different kind of base isolation systems (BIS) is usually represented as a bi-linear hysteretic force. For practical design purposes, this bi-linear hysteric force is usually replaced by an equivalent linear force by using and equivalent stiffness, k_{BIS}, which is given by:

$$k_{BIS} = \frac{F^+ - F^-}{\Delta^+ - \Delta^-} \tag{1}$$

where F^+ and F^- are the positive and negative forces at test displacements Δ^+ and Δ^-, respectively. Thus, the k_{BIS} is the slope of the peak-to-peak values of the hysteresis loop as shown in Figure 1 (Matsagar & Jangid, 2004).

According to Matsagar and Jangid (2004), the effective viscous damping of the base isolator calculated for each cycle of loading is specified as:

$$\xi_{BIS} = \frac{2}{\pi}\left(\frac{E_{loop}}{k_{BIS}\left(|\Delta^+| + |\Delta^-|\right)^2}\right) \tag{2}$$

where E_{loop} is the energy dissipation per cycle of loading. At a specified design isolation displacement, D, the effective stiffness and damping ratio for a bi-linear system are expressed by:

$$k_{BIS} = k_{PY} + \frac{Q}{D} \tag{3}$$

$$\xi_{BIS} = \frac{4Q(D-q)}{2\pi k_{BIS} D^2} \tag{4}$$

where k_{PY} is the post-yield stiffness, Q is the characteristic strength and q is the yield displacement of the BIS. Equations (1) to 4 are valid for base isolators subjected to large deformations, such as those induced by earthquakes, and may not necessarily apply under wind loads. However, in regions with both seismic and wind hazards, base isolators are always designed for the seismic case, as the primary objective of these devices is to decouple the building from ground motion.

As already mentioned above, a BIS can exhibit hysteretic and stiffening behavior at large deformation, however, the restoring force developed in the bearing is usually represented as a linear force. Considering a linear behavior, the restoring force of the BIS in time domain is given by:

$$F_{BIS}(t) = c_{BIS}\dot{u}_{BIS}(t) + k_{BIS}u_{BIS}(t) \tag{5}$$

where c_{BIS}, k_{BIS} and u_{BIS} are the damping coefficient, spring constant and lateral displacement of the BIS, respectively. Accordingly, k_{BIS} and c_{BIS} are given by:

$$k_{BIS} \approx m_T\left(\frac{2\pi}{T_{BIS}}\right)^2 \tag{6}$$

$$c_{BIS} = 2\xi_{BIS}m_T\left(\frac{2\pi}{T_{BIS}}\right) \tag{7}$$

where ξ_{BIS} is the damping ratio of the BIS; T_{BIS} is the isolation period of vibration, which is usually greater than 3 times the fundamental period of vibration of the fixed-base building (Naeim & Kelly, 1999); and m_T is the total mass of the structure, which is given by:

$$m_T = m_{BIS} + \sum_{j=1}^{N} m_j \tag{8}$$

where m_{BIS} is the mass of the BIS, m_j is the mass of the jth story of the building and N is the total number of stories.

A N-story base-isolated high-rise building with TMDIs can be schematically be represented as shown in Figure 2, where the bending and shear stiffnesses of the structure are represented by the shear wall and shear building, respectively. In this way, the lateral deformation of the structure is completely determined by a non-dimensional lateral stiffness ratio given by (Miranda & Reyes, 2002; Miranda & Taghavi, 2005):

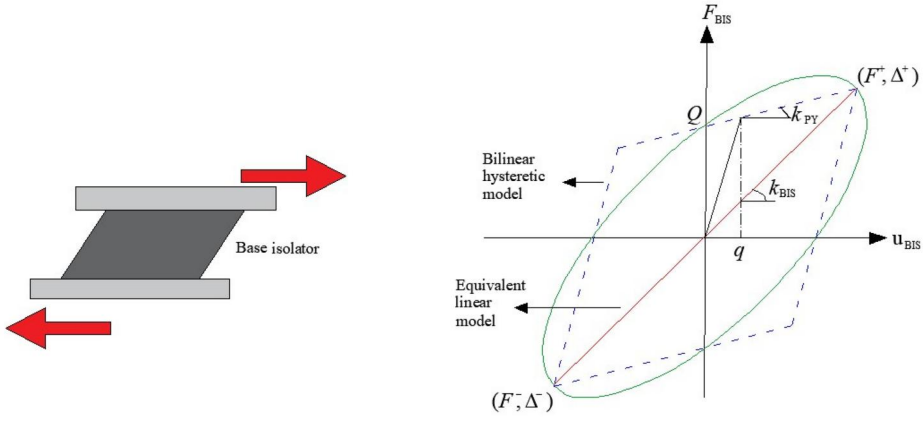

Figure 1. Equivalent restoring force of a BIS. Adapted from Matsagar and Jangid (2004).

$$\alpha = H\sqrt{\frac{GA^S}{EI}} \tag{9}$$

where H is the total height of the building, EI is the lateral flexural rigidity and GA^S is the lateral shear rigidity of the building. The extreme limits for lateral deformations are the pure flexural model ($\alpha \to 0$) and the pure shear model ($\alpha \to \infty$), respectively; however, the lateral deformation of any lateral resisting system (structural walls, braced frames, shear wall-frame buildings, tubular building systems, moment resisting frames, among others) can be adequately represented when $0 \le \alpha \le 20$. For a high-rise building with uniform mass, EI and GA^S are given by:

$$EI = \frac{4\overline{m}\pi^2 H^4}{(T_1{}^*\gamma_1)^2(\gamma_1{}^2 + \alpha^2)} \tag{10}$$

$$GA^S = \frac{4\overline{m}\pi^2\alpha^2 H^2}{(T_1{}^*\gamma_1)^2(\gamma_1{}^2 + \alpha^2)} \tag{11}$$

where $\overline{m}$ is the mass per unit length of the building; $T_1{}^*$ is the fundamental period of vibration of the fixed-base building without TMDIs, which can be computed by those empirical formulas contained in the ASCE/SEI 7-10 (2022); and γ_1 is an eigenvalue parameter related to the first mode shape of the coupled-two-beam (CTB) fixed-based continuous model without TMDIs, which can be accurately approximated by the following equation proposed by Huergo (2021):

$$\begin{aligned}\gamma_1 =& (8.0564\times10^{-10})\alpha^7 - (1.3677\times10^{-7})\alpha^6 \\ &+ (8.4444\times10^{-6})\alpha^5 - (2.5511\times10^{-4})\alpha^4 \\ &+ (4.0722\times10^{-3})\alpha^3 - (3.2706\times10^{-2})\alpha^2 \\ &+ (9.0619\times10^{-2})\alpha + 1.8603\end{aligned} \tag{12}$$

Based on Figure 2, the inerter device of the TMDI is modeled through an ideal massless mechanical element resisting the relative acceleration developing at its two ends/terminals through the inertance coefficient b (Smith, 2002). Consider a commonly used inerter device embodiment employing a rack-and-pinion mechanism to transform the translational motion into rotational motion of a flywheel (i.e. a solid spinning disk) through a gearbox shown in Figure 2. According to Smith (2002), the inertance of the jth device is given by:

$$b_j = m_f \frac{r_f{}^2}{r_{pf}{}^2}\left(\prod_{i=1}^{n}\frac{r_i{}^2}{r_{p,i}{}^2}\right) \tag{13}$$

where m_f and r_f are the mass and radius of the gyration of the flywheel, respectively; r_{pf} is the radius of gyration of the flywheel pinion; and $r_i/r_{p,i}$ is the gearing ratio of the ith stage/gear of the gearbox with n stages. In this regard, the inerter element force of a TMDI attached at j-story with second terminal connected at the same story is given by:

$$F_{\mathrm{TMDI},j}(t) = b_j\left[\ddot{u}_{\mathrm{TMDI},j}(t) - \ddot{u}_j(t)\right] \tag{14}$$

where $\ddot{u}_{\mathrm{TMDI},j}(t)$ is the acceleration of the jth TMDI and $\ddot{u}_j(t)$ is the acceleration of the jth story.

Accordingly, the sketch shown in Figure 2 can be reduced to the CTB model shown in Figure 3, where $L_j(t)$ is the height of the jth story, $F_j(t)$ is the lateral wind force at jth story; $k_j^a \to \infty$ is the lateral stiffness of the jth axially

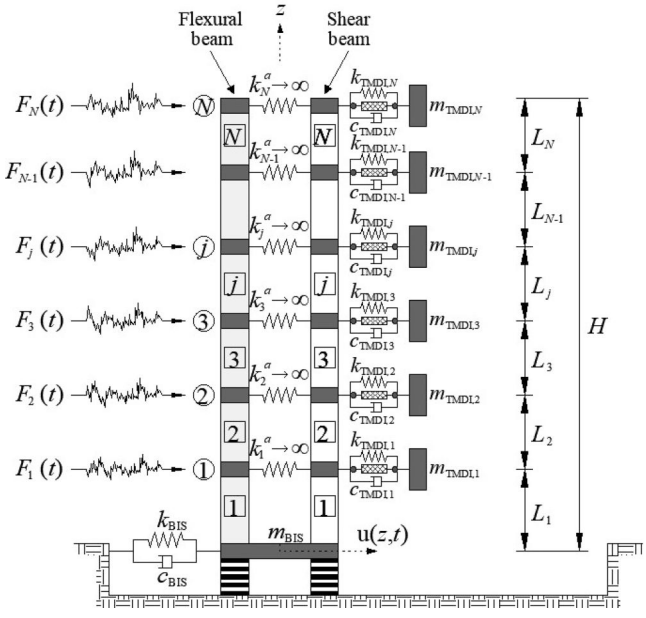

Figure 3. Base-isolated CTB model with TMDI subjected to lateral wind loads.

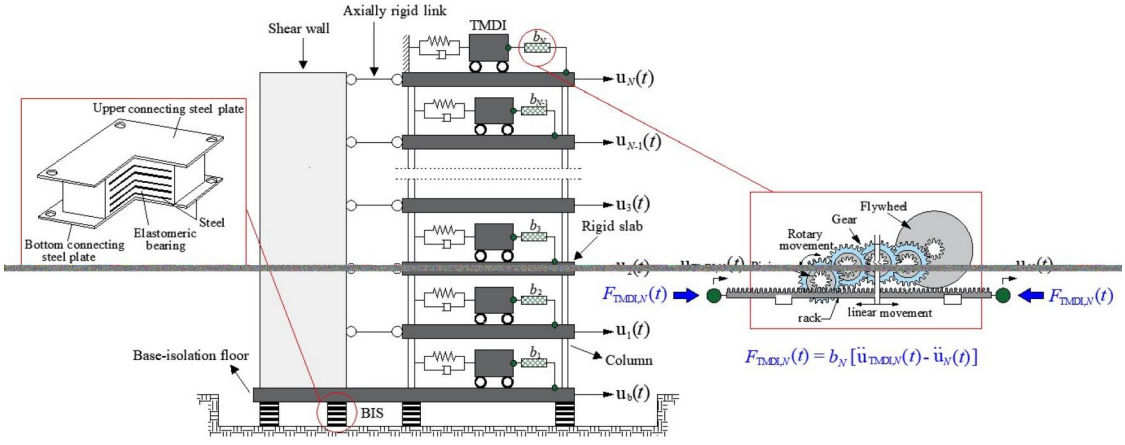

Figure 2. Sketch of a base-isolated N-story shear wall-frame building with TMDI.

rigid link, which allows the parallel coupling between flexural and shear deformations; and m_{TMDI}, k_{TMDI} and c_{TMDI} are the mass, spring stiffness and damping coefficient of the jth TMDI, respectively, which are given by:

$$m_{\mathrm{TMDI},j} = \mu_j m_{\mathrm{SDOF}} + b_j = m_{\mathrm{SDOF}}\left(\mu_j + \beta_j\right) \tag{15}$$

$$k_{\mathrm{TMDI},j} = {w_{\mathrm{TMDI},j}}^2 m_{\mathrm{TMDI},j} = \frac{4\pi^2 m_{\mathrm{TMDI},j}}{{T_{\mathrm{TMDI},j}}^2} \tag{16}$$

$$c_{\mathrm{TMDI},j} = 2 m_{\mathrm{TMDI},j} w_{\mathrm{TMDI},j} \xi_{\mathrm{TMDI},j} \tag{17}$$

where:

$$b_j = \beta_j m_{\mathrm{SDOF}} \tag{18}$$

$w_{TMDI,j}$ and $T_{TMDI,j}$ are the angular frequency and period of vibration of the jth TMDI, respectively; μ_j is the non-dimensional mass ratio of the jth TMDI, ranging from 1/50 to 1/15 for the pre-design stage of a typical tuned mass damper (Bachmann et al., 1995); b_j is the constant of proportionality of jth TMDI that attains mass units and fully characterizes the behavior of the inerter (see Equation 13); and β_j and $\xi_{TMDI,j}$ are the non-dimensional inerter ratio and damping ratio of the jth TMDI, respectively, which are to be limited to maximum values of 0.8 to avoid unrealistically high viscous damping coefficients and inertance for the considered structure (Petrini et al., 2020). On the other hand, m_{SDOF} is the equivalent mass of the primary system, that is, a single degree of freedom system (SDOF) equivalent mass for the base-isolated building without TMDIs, which is given by:

$$m_{\mathrm{SDOF}} = \frac{\{\phi_i\}^T \{M\} \{\phi_i\}}{\left(\phi_{i,0} + \phi_i^j\right)^2} \tag{19}$$

where $\{\phi_i\}^T\{M\}\{\phi_i\}$ is the generalized mass of the ith lateral mode of vibration of the base-isolated building without TMDIs; $\{\phi_i\}$ is the modal amplitudes vector of the ith lateral mode of vibration of the base-isolation building without TMDIs; $\{M\}$ is the mass matrix of the of the base-isolated building without TMDIs; $\phi_{i,0} + \phi_i^j$ is the total modal amplitude of the ith lateral mode of vibration at the attachment point of the jth TMDI; $\phi_{i,0}$ is the lateral modal amplitude of the ith lateral mode of vibration at the base-isolation floor; and ϕ_i^j is the lateral modal amplitude of the ith lateral mode of vibration at the attachment point of the jth TMDI.

For practical design engineering purposes, the angular frequency and period of vibration of the jth TMDI are given by:

$$w_{\mathrm{TMDI},j} = \nu_{\mathrm{TMDI},j} w_1 \rightarrow T_{\mathrm{TMDI},j} = \frac{T_1}{\nu_{\mathrm{TMDI},j}} \tag{20}$$

where $w_{\mathrm{TMDI},j}$ and $T_{\mathrm{TMDI},j}$ are the angular frequency and period of vibration of the jth TMDI, respectively; w_1 and T_1 are the angular frequency and period of the fundamental mode of vibration of the base-isolated building without TMDIs, respectively; and $\nu_{\mathrm{TMDI},j}$ is the frequency ratio of the jth TMDI, which may be chosen in the range of 0.8 to 1.2 to ensure tuning of the TMDI with the primary structure (Petrini et al., 2020).

Based on the CTB model with soil-structure interaction (Huergo & Hernández, 2020), the rigid body motion of the building caused by base isolation can be incorporated if the base rotational motion is neglected. In this way, the $4N+2$ equations of motion of the base-isolated CTB model with N TMDIs (see Figure 3) are given by:

$$[M_{\mathrm{CTB}}]\left\{\ddot{u}_{\mathrm{CTB}}(t)\right\} + [C_{\mathrm{CTB}}]\left\{\dot{\mathrm{u}}_{\mathrm{CTB}}(t)\right\} + [K_{\mathrm{CTB}}]\left\{\mathrm{u}_{\mathrm{CTB}}(t)\right\} = \left\{F_{\mathrm{CTB}}(t)\right\} \tag{21}$$

where $[M_{\mathrm{CTB}}]$, $[K_{\mathrm{CTB}}]$ and $[C_{\mathrm{CTB}}]$ are the mass matrix, stiffness matrix and damping matrix of the CTB model, respectively; $\left\{\mathrm{u}_{\mathrm{CTB}}(t)\right\}$ is a vector containing the lateral displacements of all degree of freedom systems; and $\left\{F_{\mathrm{CTB}}(t)\right\}$ is the external force vector.

The mass matrix of the CTB model with N TMDIs can be defined as:

$$[M_{\mathrm{CTB}}] = \begin{bmatrix} \left[M_\Psi^F\right] & [0]_{(2N+1)\times(2N+1)} \\ [0]_{(2N+1)\times(2N+1)} & \left[M_\Psi^S\right] \end{bmatrix} + \begin{bmatrix} [b^F] & [0]_{(2N+1)\times(2N+1)} \\ [0]_{(2N+1)\times(2N+1)} & [b^S] \end{bmatrix} \tag{22}$$

where:

$$\left[M_\Psi^F\right] = \begin{bmatrix} \frac{1}{2}\left(m_{\mathrm{T}} + \sum_{j=1}^{N} m_{\mathrm{TMDI},j}\right) & \{1\}_{1xN}\left[M_\Delta^F\right]_{N\times N} & \{1\}_{1xN}\left[M_{\mathrm{TMDI}}^F\right]_{N\times N} \\ \left[M_\Delta^F\right]_{N\times N}\{1\}_{N\times 1} & \left[M_\Delta^F\right]_{N\times N} & [0]_{N\times N} \\ \left[M_{\mathrm{TMDI}}^F\right]_{N\times N}\{1\}_{N\times 1} & [0]_{N\times N} & \left[M_{\mathrm{TMDI}}^F\right]_{N\times N} \end{bmatrix} \tag{23}$$

$$\left[M_\Psi^S\right] = \begin{bmatrix} \frac{1}{2}\left(m_{\mathrm{T}} + \sum_{j=1}^{N} m_{\mathrm{TMDI},j}\right) & \{1\}_{1xN}\left[M_\Delta^S\right]_{N\times N} & \{1\}_{1xN}\left[M_{\mathrm{TMDI}}^S\right]_{N\times N} \\ \left[M_\Delta^S\right]_{N\times N}\{1\}_{N\times 1} & \left[M_\Delta^S\right]_{N\times N} & [0]_{N\times N} \\ \left[M_{\mathrm{TMDI}}^S\right]_{N\times N}\{1\}_{N\times 1} & [0]_{N\times N} & \left[M_{\mathrm{TMDI}}^S\right]_{N\times N} \end{bmatrix} \tag{24}$$

$$\left[M_{\mathrm{TMDI}}^F\right]_{N\times N} = \left[M_{\mathrm{TMDI}}^S\right]_{N\times N} = \frac{1}{2}\begin{bmatrix} m_{\mathrm{TMDI},1} & & \\ & \ddots & \\ & & m_{\mathrm{TMDI},N} \end{bmatrix} \tag{25}$$

$\left[M_\Delta^F\right]$ is the lumped mass matrix of the flexural beam, $\left[M_\Delta^S\right]$ is the lumped mass matrix of the shear beam, and $[b^F] = [b^S]$ is a matrix containing the inertance coefficients of the TMDIs. If the second terminals of the TMDIs are connected to the same story where the device are attached (see Figure 3), then the TMDIs act as traditional TMDs ($b_j = 0$ for $j = 1,2,3,\ldots,N$), where the matrix of the inertance coefficients is given by:

$$[b^F] = [b^S] = [0]_{(2N+1)\times(2N+1)} \tag{26}$$

On the other hand, if the second terminals of the TMDIs are connected to different stories, then the matrix of the inertance coefficients must be related to the degrees of freedom of both terminals. For example, in the case of a N-story building with a single TMDI at the N^{th} story with the second terminal linked to the N-1 story, the matrix $[M_{\mathrm{CTB}}]$ will be of size $2N+4$, then the inerter element force of the TMDI and the matrix of the inertance coefficients would be

given by:

$$F_{\mathrm{TMDI},N}(t) = b\left[\ddot{u}_{\mathrm{TMDI},N}(t) - \ddot{u}_{N-1}(t)\right] \tag{27}$$

$$[b^F] = [b^S] = \frac{1}{2}\begin{bmatrix} \sum_{j=1}^{N} b_{jj} & \{1\}_{1xN}[b]_{N\times N} & 0 \\ [b]_{N\times N}\{1\}_{N\times 1} & [b]_{N\times N} & -[b]_{N\times N}\{1\}_{N\times 1} \\ 0 & -\{1\}_{1xN}[b]_{N\times N} & 0 \end{bmatrix} \tag{28}$$

where:

$$[b]_{N\times N} = \begin{bmatrix} 0 & & & & \\ & 0 & & & \\ & & 0 & & \\ & & & \ddots & \\ & & & & b \\ & & & & & 0 \end{bmatrix} \tag{29}$$

and b_{jj} is the element in row j and column j of matrix $[b]_{N\times N}$. It is important to mention that the terms $m_{\mathrm{TMDI},j}$ in Equations (23) to (25) already include the inertance coefficients, meaning they should be calculated based on Equation (15). The TMDI is designed to add an additional mass and an inerter (b) to control vibrations.

The stiffness matrix and damping matrix of the CTB model with N TMDIs can be defined as:

$$[K_{\mathrm{CTB}}] = \begin{bmatrix} [K_\Psi^F] & [K_\Psi^C] \\ [K_\Psi^C] & [K_\Psi^S] \end{bmatrix} \tag{30}$$

$$[C_{\mathrm{CTB}}] = \begin{bmatrix} [C_\Psi^F] & [0]_{(2N+1)\times(2N+1)} \\ [0]_{(2N+1)\times(2N+1)} & [C_\Psi^S] \end{bmatrix} \tag{31}$$

where:

$$[K_\Psi^F] = \begin{bmatrix} \frac{k_{\mathrm{BIS}}}{2} & \{0\}_{1\times N} & \{0\}_{1\times N} \\ \{0\}_{N\times 1} & [K_\Delta^F]_{N\times N} + [K^A] + [K_{\mathrm{TMDI}}^F]_{N\times N} & -[K_{\mathrm{TMDI}}^F]_{N\times N} \\ \{0\}_{N\times 1} & -[K_{\mathrm{TMDI}}^F]_{N\times N} & [K_{\mathrm{TMDI}}^F]_{N\times N} \end{bmatrix} \tag{32}$$

$$[K_\Psi^S] = \begin{bmatrix} \frac{k_{\mathrm{BIS}}}{2} & \{0\}_{1\times N} & \{0\}_{1\times N} \\ \{0\}_{N\times 1} & [K_\Delta^S]_{N\times N} + [K^A] + [K_{\mathrm{TMDI}}^S]_{N\times N} & -[K_{\mathrm{TMDI}}^S]_{N\times N} \\ \{0\}_{N\times 1} & -[K_{\mathrm{TMDI}}^S]_{N\times N} & [K_{\mathrm{TMDI}}^S]_{N\times N} \end{bmatrix} \tag{33}$$

$$[K_\Psi^C] = \begin{bmatrix} 0 & \{0\}_{1\times N} & \{0\}_{1\times N} \\ \{0\}_{N\times 1} & -[K^A] & [0]_{N\times N} \\ \{0\}_{N\times 1} & [0]_{N\times N} & [0]_{N\times N} \end{bmatrix} \tag{34}$$

$$[K^A] = \begin{bmatrix} k_1^a \to \infty & & \\ & \ddots & \\ & & k_N^a \to \infty \end{bmatrix} \tag{35}$$

$$[K_{\mathrm{TMDI}}^F]_{N\times N} = [K_{\mathrm{TMDI}}^S]_{N\times N} = \frac{1}{2}\begin{bmatrix} k_{\mathrm{TMDI},1} & & \\ & \ddots & \\ & & k_{\mathrm{TMDI},N} \end{bmatrix} \tag{36}$$

$$[C_\Psi^F] = \begin{bmatrix} \frac{c_{\mathrm{BIS}}}{2} & \{0\}_{1\times N} & \{0\}_{1\times N} \\ \{0\}_{N\times 1} & [C_\Delta^F]_{N\times N} + [C_{\mathrm{TMDI}}^F]_{N\times N} & -[C_{\mathrm{TMDI}}^F]_{N\times N} \\ \{0\}_{N\times 1} & -[C_{\mathrm{TMDI}}^F]_{N\times N} & [C_{\mathrm{TMDI}}^F]_{N\times N} \end{bmatrix} \tag{37}$$

$$[C_\Psi^S] = \begin{bmatrix} \frac{c_{\mathrm{BIS}}}{2} & \{0\}_{1\times N} & \{0\}_{1\times N} \\ \{0\}_{N\times 1} & [C_\Delta^S]_{N\times N} + [C_{\mathrm{TMDI}}^S]_{N\times N} & -[C_{\mathrm{TMDI}}^S]_{N\times N} \\ \{0\}_{N\times 1} & -[C_{\mathrm{TMDI}}^S]_{N\times N} & [C_{\mathrm{TMDI}}^S]_{N\times N} \end{bmatrix} \tag{38}$$

$$[C_{\mathrm{TMDI}}^F]_{N\times N} = [C_{\mathrm{TMDI}}^S]_{N\times N} = \frac{1}{2}\begin{bmatrix} c_{\mathrm{TMDI},1} & & \\ & \ddots & \\ & & c_{\mathrm{TMDI},N} \end{bmatrix} \tag{39}$$

In Equations (32), (33), (37), and (38), the lateral stiffness matrix and damping matrix of the flexural beam are $[K_\Delta^F]$ and $[C_\Delta^F]$, respectively; whereas the matrices for the shear beam are represented by $[K_\Delta^S]$ and $[C_\Delta^S]$, respectively. Based on the traditional finite element assembly technique and Rayleigh damping model, Huergo and Hernández (2019) described in detail the assembly procedure of the mass matrix, stiffness matrix and damping matrix related to the decoupled beams.

The vector containing the external loads for the CTB model with N TMDs is given by:

$$\{F_{\mathrm{CTB}}(t)\} = \begin{bmatrix} \{F_\Psi^F(t)\} & \{F_\Psi^S(t)\} \end{bmatrix}^T \tag{40}$$

where:

$$\{F_\Psi^F(t)\} = \{F_\Psi^S(t)\} = \frac{1}{2}\left\{ \sum_{j=1}^{N} F_j(t) \quad F_1(t) \quad \dots \quad F_N(t) \quad \{0\}_{N\times 1} \right\} \tag{41}$$

and $F_j(t)$ is the lateral wind load in time domain at jth story. For the specific case in which the base-isolated CTB model with TMDI is subjected to seismic loads, Equation (41) must be changed by:

$$\{F_\Psi^F(t)\} = -\ddot{u}_g(t)\left\{ \frac{1}{2}(m_T + \sum_{j=1}^{N} m_{\mathrm{TMDI},j})\, m_1^F \dots m_N^F \frac{m_{\mathrm{TMDI},1}}{2} \dots \frac{m_{\mathrm{TMDI},N}}{2} \right\} \tag{42}$$

$$\{F_\Psi^S(t)\} = -\ddot{u}_g(t)\left\{ \frac{1}{2}(m_T + \sum_{j=1}^{N} m_{\mathrm{TMDI},j}) \quad m_1^S \quad \dots \quad mNS\, \frac{m_{\mathrm{TMDI},1}}{2} \dots \frac{m_{\mathrm{TMDI},N}}{2} \right\} \tag{43}$$

where $\ddot{u}_g(t)$ is the seismic ground acceleration, m_j^F is the lumped mass at the jth node of the flexural beam and m_j^S is the lumped mass at the jth node of the shear beam. The lumped masses of each decoupled beam are equivalent to half of the mass of the building's floor.

Finally, the displacement vector in time domain for the CTB model with N TMDs can be expressed as:

$$\{u_{\mathrm{CTB}}(t)\} = \begin{bmatrix} \{u_\Psi^F(t)\} & \{u_\Psi^S(t)\} \end{bmatrix}^T \tag{44}$$

where:

$$\left\{u_{\Psi}^{F}(t)\right\} = \left\{u_{\Psi}^{S}(t)\right\} = \frac{1}{2}\left\{ u_{BIS}(t) \quad u_1(t) \right.$$
$$\left. \cdots u_N(t) u_{TMDI,1}(t) \cdots u_{TMDI,N}(t) \right\} \tag{45}$$

For the purpose of assessing the global motion of the structure, ensuring the reliability of the isolation system, and addressing construction joints or content design, it is essential to evaluate the total displacement of the system, which can be obtained by summing the displacement of the story and the displacement of the base isolator.

3. Numerical study

In this section, a parametric analysis was carried out to illustrate the feasibility, effectiveness and consideration of the TMDI in the wind-induced vibration mitigation of base-isolated high-rise buildings with different lateral resisting systems.

3.1. Benchmark base-isolated building

There is a need to compare and assess the performance of base-isolation systems for different lateral deformations related to the great diversity of lateral resisting systems used in tall buildings. Therefore, the concept of a benchmark problem has been planned, that is, a standardized building previously used in scientific literature to assess the performance, accuracy and efficiency of the new model that incorporates base isolators and TMDI. In this way, the benchmark building (see Figure 4) is based on a rectangular 37-story building located in Mexico City with a uniform mass equal to 235664 kg/m and dimensions of 44 × 22 m x 144.24 m, which has the peculiarity of being structured based on two different lateral resisting systems in each direction for approximately the same fundamental period of vibration, that is, $T_1^* \approx 3.5$s for both translational directions. For the *xz* plane, moment resisting frames are related to a shear pure behavior ($\alpha \to \infty$), whereas the lateral behavior of braced frames and shear walls of the *yz* plane are mostly dominated by the flexural stiffness ($\alpha = 3.5$). For the purpose of further consultation, the mechanical properties of each structural element are described in detail by Huergo et al. (2020).

A seismic record with high energy content at high frequencies would cause resonant amplification of the dynamic response of the benchmark building. For this reason, it was considered that the benchmark building was subjected to the horizontal ground accelerations recorded at station Central-de-Abastos-Frigorífico (CDAF) during the Mexico City earthquake of September 19, 1985 (see Figure 5a). Based on a critical damping ratio equal to 5%, Figure 5(b) shows that the resonance response will occur for buildings with a period of vibration of 3.05 s. In addition, Figure 5(b) shows that the input energy per unit mass for *xz* plane and *yz* plane are 1.25 m^2/s^2 and 2.10 m^2/s^2, respectively, on the other hand, the input energy per unit mass is 0.18 m^2/s^2 for a target period of the BIS equal to 7 s. The earthquake shown in Figure 5 is likely to cause non-linear effects on the structure, however, the behavior of the structure was assumed to be linear since the objective of this section is

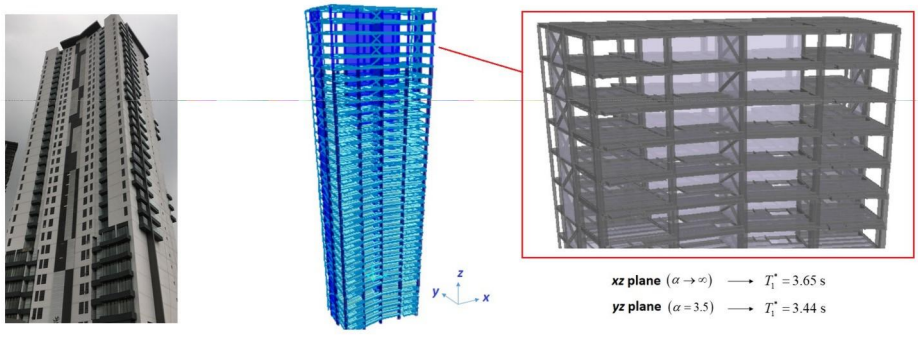

(a) General view (b) 3D finite element model

Figure 4. Benchmark building.

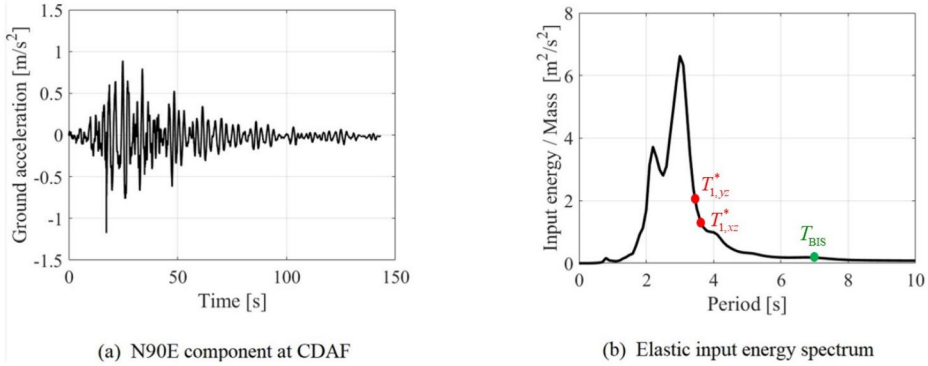

(a) N90E component at CDAF (b) Elastic input energy spectrum

Figure 5. Mexico City earthquake of september 19, 1985: station CDAF. Adapted from Huergo et al. (2020).

only to have a starting point of the general effects of the base isolator on the building for the design objective of the building (seismic loading).

The mass of the BIS was considered equal to the lumped mass at any intermediate story of the building. In order to avoid the resonant dynamic response, a target period of vibration equal to 7 s was defined for both directions of the isolated building. On the other hand, an increase in the damping of the base isolation system (BIS) is beneficial to reduce the lateral displacements of the device. However, this increase reduces the effectiveness of the isolation, which usually results in an increase in the lateral dynamic response of the superstructure. For seismic applications, the modal damping ratio of the first mode of the superstructure usually ranges between 0.02 and 0.05, on the other hand, the modal damping ratio of the BIS usually ranges between 0.10 and 0.40. Therefore, Table 2 shows the mechanical properties of the BIS for 4 different damping values, whereas Figure 6 and Table 3 show the undamped modes of vibration of both the fixed-base model and base-isolated building.

For the fixed base building, Table 3 shows that the higher modes of vibration contribute to the lateral deformation and movement of the superstructure when α is close to 0 (pure flexural behavior). On the other hand, the first mode of vibration of the base-isolated building is the only one that contributes to the lateral deformation regardless of the value of α.

Table 2. Mechanical properties of the base-isolation system for both lateral directions.

m_T[Gg]	T_{BIS}[s]	m_{BIS}[Gg]	k_{BIS}[kN/m]	ξ_{BIS}	c_{BIS}[kN s/m]
34.45	7	0.9187	27757	0.10	6184.8
				0.20	12370
				0.30	18554
				0.40	24739

The peak insterstory drift demands are usually used to check the ultimate limit state under seismic loads, which are usually located in the lower levels for low-rise buildings (pure shear behavior). However, the peak interstory drift ratio (IDR) is located on the upper levels for high-rise buildings where the flexural deformation is as significant as the shear deformation. On the other hand, total peak floor accelerations are useful for design of building contents. For that reason, Figures 7 and 8 show the peak IDR and total peak floor accelerations for both the fixed-base case and base-isolated building under the seismic load shown in Figure 5 and the BIS parameters shown in Table 2.

Based on Figure 7, a low damping BIS reduces the damage (peak IDR) of the benchmark building by up to 83% in the *xz* plane and up to 85% in the *yz* plane, however, the displacements of the base isolator will be greater as ξ_{BIS} decreases. On the other hand, Figure 8 shows that a low damping BIS reduces the total peak acceleration of the benchmark building (content design) by up 50% in the *xz* plane and up to 67% in the *yz* plane. It is evident to note that for the case without BIS, the total peak accelerations increase as the lateral deformation of the building is close to pure flexural behavior (*yz* plane) due to the participation of higher modes of vibration. In addition, it is verified that an increase in the damping of the BIS decreases the lateral displacement of the device but increases the lateral dynamic response of the superstructure.

Since no model in the scientific literature incorporates base isolation into the CTB model, it is necessary to validate it based on an existing one. Low-rise buildings are typically modeled using the classical model consisting on a base-isolated multi-degree-of-freedom (MDOF) shear model, as there was previously no need to include base isolation in high-rise buildings. For this reason, it is possible to validate the CTB model by comparing the *xz* plane of the benchmark building with the classical base-isolated MDOF shear model (Stanikzai et al., 2020). Accordingly, Figure 9 shows

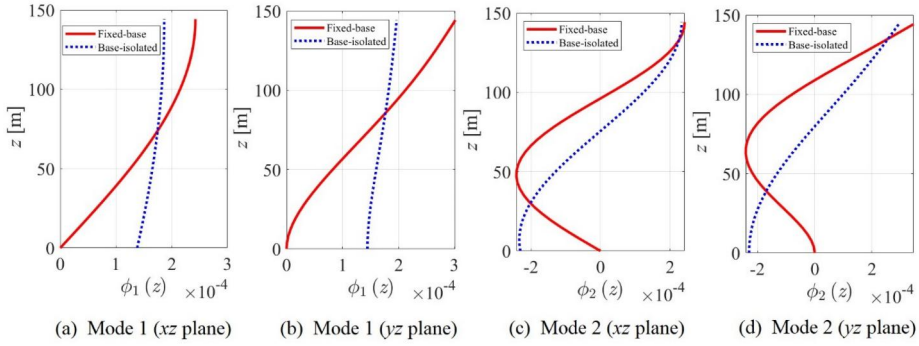

Figure 6. Modes of vibration of the undamped base-isolated benchmark building.

Table 3. Periods and effective modal mass of the benchmark building: fixed-base vs base-isolated.

	Period [s]				Effective modal mass [%]			
	xz plane		*yz* plane		*xz* plane		*yz* plane	
Mode	Fixed-base	Base-isolated	Fixed-base	Base-isolated	Fixed-base	Base-isolated	Fixed-base	Base-isolated
1	3.65	7.76	3.44	7.59	81.03	99.27	67.99	99.02
2	1.22	1.74	0.89	1.90	8.98	0.44	13.25	0.68

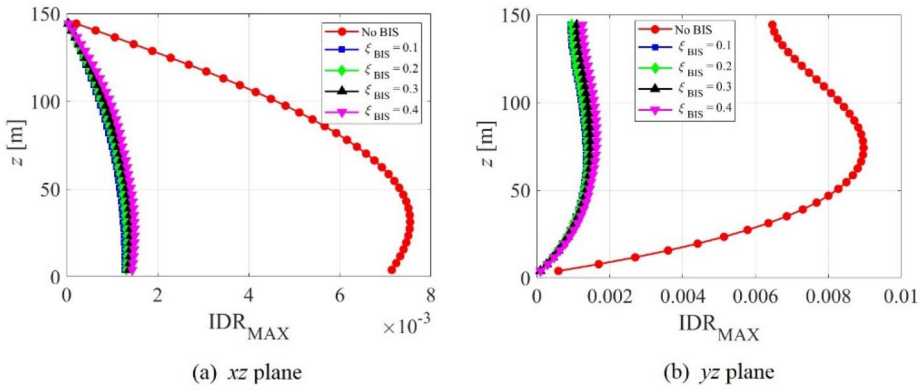

Figure 7. Peak interstory drift ratios of the benchmark building: Mexico city earthquake of september 19, 1985 (station CDAF).

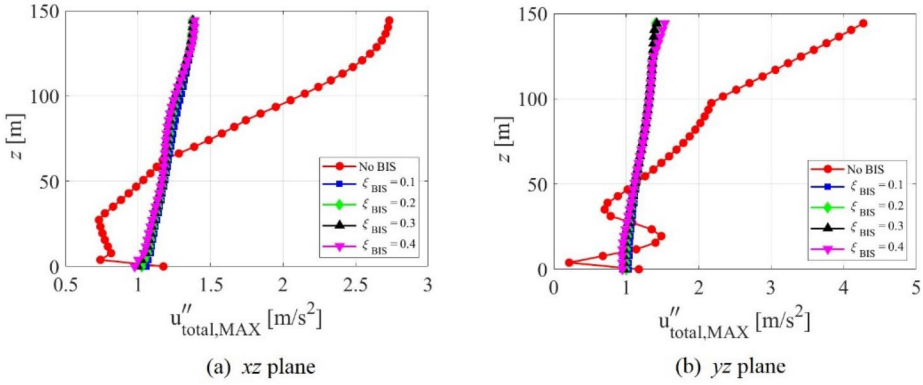

Figure 8. Total peak floor accelerations of the benchmark building: Mexico city earthquake of september 19, 1985 (station CDAF).

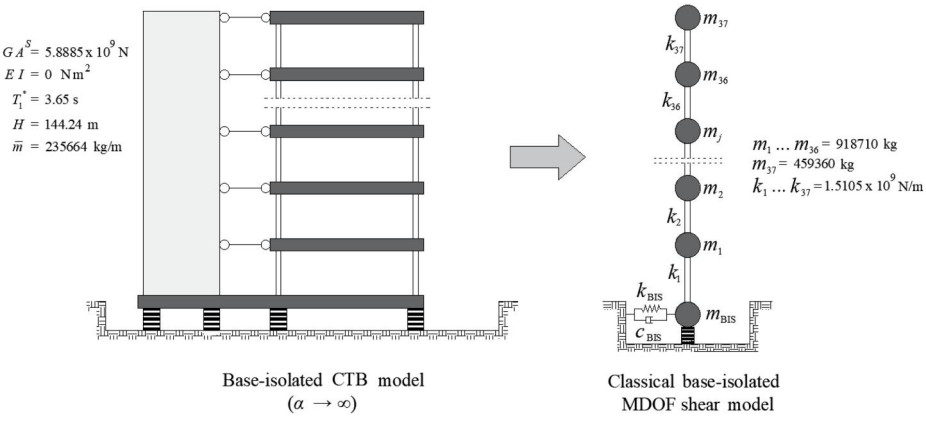

Figure 9. Validation scheme for the proposed base-isolated CTB model: *xz* plane of the benchmark building.

the equivalent classical base-isolated MDOF shear model for the *xz* plane of the benchmark building, which undergoes lateral deformation in pure shear ($\alpha \to \infty$).

The equations of motion for the classical base-isolated MDOF model were assembled based on the work developed by Stanikzai et al. (2020). These equations of motion were solved considering the seismic load of Figure 5 and the mechanical properties of the base isolators of Table 2. Table 4 demonstrates that the base-isolated CTB model ($\alpha \to \infty$) produces practically the same dynamic responses as the classical model, thereby validating the numerical development presented in Section 2. In addition, the first two periods of vibration of the classical base-isolated model related to the benchmark building were also $T_1 = 7.76$s and $T_1 = 1.74$s, respectively.

3.2. Wind load simulation

In the atmospheric boundary layer (see Figure 10a), the turbulence intensity in the along-wind direction, $I_u(z)$, is determined by the roughness length, z_o, that is, the equivalent height at which the wind speed theoretically becomes zero in the absence of wind-slowing obstacles. Accordingly, the gradient height, z_g, is the height above ground where surface friction has a negligible effect on wind speed, therefore,

Table 4. Validation of the base-isolated CTB model: seismic response of benchmark building (*xz* plane).

		ξ_{BIS}			
Response	Model	0.1	0.2	0.3	0.4
IDR_{max}	Classical base-isolated MDOF shear model	0.001275	0.001323	0.001404	0.001495
	Base-isolated CTB model ($\alpha \to \infty$)	0.001302	0.001394	0.001502	0.001610
$u''_{total,MAX}$ [m/s^2]	Classical base-isolated MDOF shear model	1.3767	1.3723	1.3787	1.3901
	Base-isolated CTB model ($\alpha \to \infty$)	1.4144	1.4112	1.4238	1.4415

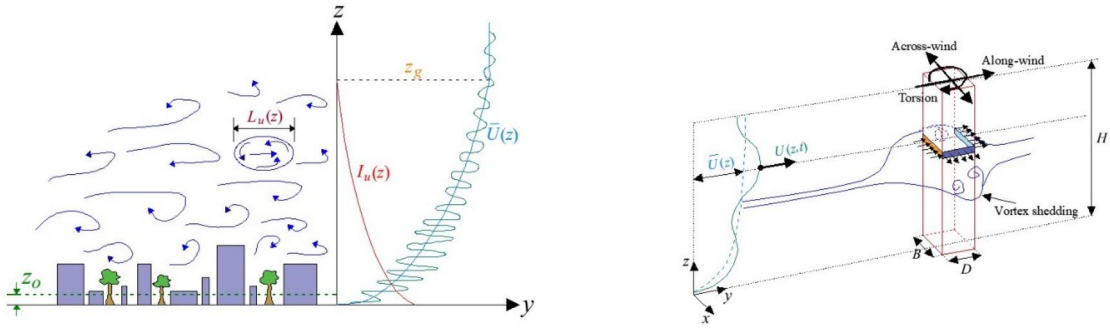

(a) Sketch of atmospheric boundary layer (b) Wind-induced vibration of tall buildings

Figure 10. Turbulent wind effects on tall buildings.

Table 5. Wind profile properties for the benchmark building (CFE, 2020).

City	Average daily minimum temperature [°C]	Barometric pressure [mmHg]	Latitude [°]	z_o[m]	Annual probability [%]	Averaging time [s]	$\bar{U}$(10m) [m/s]
Mexico City	0	586	19.404°	0.3	10	600	16.65

Table 6. Wind load simulation parameters for the benchmark building.

	Along-wind loads		Across-wind loads	
Parameter	*xz* plane	*yz* plane	*xz* plane	*yz* plane
D/*B*	2	0.5	0.5	2
Drag coefficient (CFE, 2020)	1.1	1.45	–	–
Lift coefficient (Liang et al, 2002)	–	–	0.1819	0.5820
Strouhal number (Liang et al., 2002)	–	–	0.0940	0.0670
Wind profile (Harris & Deaves, 1981)	Corrected logarithmic	Corrected logarithmic	Corrected logarithmic	Corrected logarithmic
Power Spectral Density (PSD) Function	ESDU (2001)	ESDU (2001)	Liang et al. (2002)	Liang et al. (2002)
Aerodynamic admittance function	Vickery (1968)	Vickery (1968)	–	–
Root-coherence function	Krenk (1996)	Krenk (1996)	Davenport (1962)	Davenport (1962)
Vertical decay constant	5 (Krenk, 1996)	5 (Krenk, 1996)	1.26 (Huergo et al., 2022)	1.81 (Huergo et al., 2022)

the longitudinal component of the wind velocity within the atmospheric boundary layer is composed by a mean wind velocity, $\overline{U}(z)$, and a fluctuating part, $u(z,t)$. Under the action of a turbulent wind flow, tall buildings are subjected to vibrations in along-wind, across-wind and torsional directions (see Figure 10b). The along-wind load is the result of the combined effect of the windward pressure and the leeward pressure, whereas the across-wind load is the result of the suction force generated by the vortex shedding in the plane normal to the wind. Vortex shedding can induce significant amplitude vibrations when the vortex frequency is in resonance with the fundamental frequency of vibration of the structure.

Based on Figure 10(b), the drag force (along-wind load) and lift force (across-wind load) at the *j*th story are, respectively, given by:

$$F_D(z_j,t) = \frac{1}{2}\rho_a A_j C_D \left[\overline{U}(z_j) + u(z_j,t)\right]^2 \tag{46}$$

$$F_L(z_j,t) = \frac{1}{2}\rho_a A_j \overline{F}_L(z_j,t) \left[\overline{U}(z_j)\right]^2 \tag{47}$$

where ρ_a is the density of air; A_j is the area of impact of the wind force on the façade of the *j*th story, which can be assumed in the same way as the story masses are lumped; C_D is the drag coefficient, which can be obtained from the Mexican wind code (CFE, 2020); $\overline{U}(z_j)$ is the mean wind velocity at z_j; $u(z_j,t)$ is the turbulent component of the along-wind velocity; and $\overline{F}_L(z_j,t)$ is the non-dimensional across-wind force at height z_j at time t.

In Equations (46) and (47), $u(z_j,t)$ and $\overline{F}_L(z_j,t)$ are stationary Gaussian multidimensional stochastic processes that can be simulated in time domain by using Monte Carlo

simulation techniques such as the Spectral Representation Method (SRM) proposed by Shinozuka et al. (1990); Gao et al., 2012; Huergo et al., 2022). For the specific case of across-wind loads, $\overline{F}_L(z_j, t)$ must be simulated based on the improved SRM (Gao et al., 2012) in order to avoid a negative definite Hermitian cross-spectral density matrix. In this way, the lateral wind loads were simulated in time domain based on all the statistical parameters recommended by Huergo et al. (2022) for along-wind and across-wind loads, which are summarized in Tables 5 and 6. In Table 6, the aerodynamic admittance function represents the relation between the gust frequency and its area of influence, therefore, it is necessary to apply a filter (aerodynamic admittance function) to the simulated values of $u(z, t)$ before converting them into drag forces by Equation (46). On the other hand, the across-wind loads, being directly simulated as a stochastic process, do not require the application of an aerodynamic admittance function, as PSD function (Liang et al., 2002) is already directly related with lift forces. In addition, root-coherence functions represent the statistical dependence between the power spectra at two different heights, which enables the simulation to be considered as a set of N homogeneous Gaussian multidimensional processes.

In general, the probabilistic dependence underlying the stochastic process describing wind loads may be well approximately by a Gaussian process. Although, the one dimensional marginal distributions are not necessarily Gaussian. Accordingly, Figure 11 shows a well-fitting simulation for the lateral wind loads for the 144-meter-tall building, where B is the width of the windward side and D is the depth of the cross section of the building (see Figure 10b). A summary of the dependence structure of the stochastic process describing wind loads may be found in the Appendix of this manuscript.

For the across-wind loads, mechanical resonance will occur when vortex shedding frequencies match natural

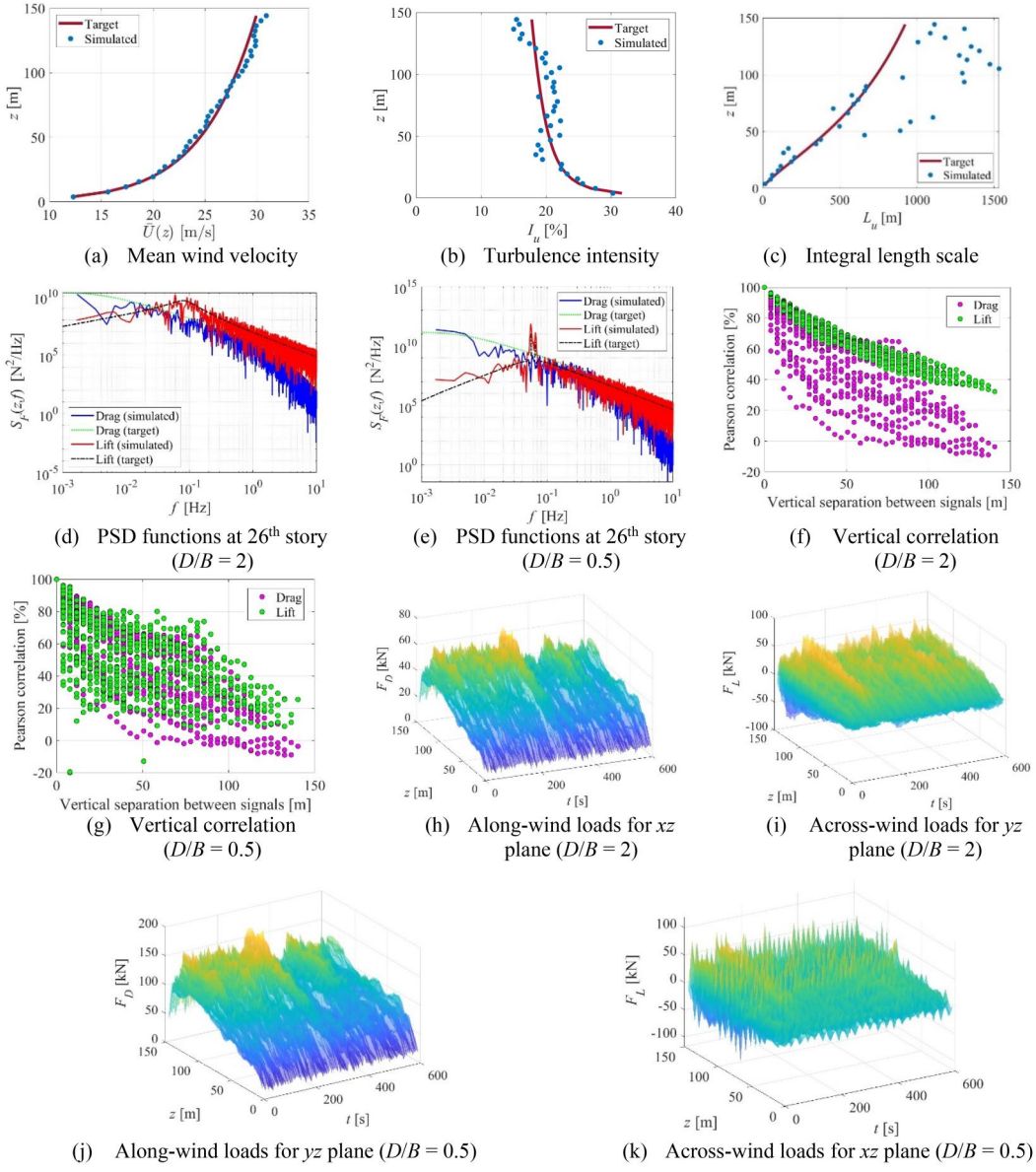

Figure 11. Statistical parameters of wind simulations.

frequency of the building. Accordingly, the critical mean wind velocity for mechanical resonance in the across-wind direction is given by:

$$\overline{U}_{crit} = \frac{B}{S_t T_{1,L}} \tag{48}$$

where B is the width of the windward side, S_t is the Strouhal number and $T_{1,L}$ is the natural period of vibration of the building in direction of lift forces (across-wind direction). Accordingly, the values of $\overline{U}_{crit}$ for xz plane and yz plane of the fixed-base benchmark building are 128.24 m/s and 95.45 m/s, respectively; whereas for xz plane and yz plane of the base-isolated case, they are 60.32 m/s and 43.26 m/s, respectively. Therefore, base isolation could drastically increase the wind-induced dynamic response of high-rise building in the across-wind direction because mechanical resonance could occur at smaller wind mean velocities in comparison with the fixed-base case. Based on Figure 11(a), it is expected that the across-wind displacements of the building in the yz plane will be much more critical than the along-wind displacements, as the mean wind velocity on the rooftop ($\approx$ 30 m/s) is very close to the critical wind velocity (43.26 m/s). Under such circumstances, the use of additional control devices could provide a practical solution to vortex shedding resonance vibration.

3.3. TMDI for wind-induced vibration control

3.3.1. Effect of mass ratio and damping ratio

As already mentioned above, the main goal of this paper is to assess the effect of TMDIs to control the along-wind and across-wind responses of base-isolated high-rise building considering different lateral resisting systems. For the purpose of this research, the analysis is limited here to LRB systems, however, the analysis scheme is equally applicable for other isolation systems by utilizing an equivalent linearization approach to account for nonlinearity. Accordingly, six different building isolator damper configurations were considered for the benchmark building (see Figure 12): (a) fixed-base building (FB), (b) fixed-base building with a top tuned mass damper inerter (FB-TTMDI), (c) base-isolated building (BI), (d) base-isolated building with a top tuned mass damper inerter (BI-TTMDI), (e) base-isolated building with a bottom tuned mass damper inerter (BI-BTMDI) and (f) base-isolated building with double tuned mass damper inerter (BI-DTMDI). Furthermore, the special case of the typical TMD ($\beta = 0$) can be examined and, to this effect, the bounds of ν and μ usually are ranged from 0.8 to 1.2 and from 0.001 to 0.01, respectively, based on real-life TMD installations tuned to the first/fundamental mode shape of high-rise buildings (Petrini et al., 2020). On the other hand, it is convenient that ξ_{TMDI} and β are limited to maximum values of 0.8 to avoid unrealistically high viscous damping coefficients and inertance for the considered structure (Petrini et al., 2020).

Based on Figure 12, the mass ratio and inertance coefficient of each TMDI were set to $\mu = 0.02$ and $\beta = 0.2$, respectively; whereas, the frequency ratio and damping ratio of each TMDI were computed by the following equations (Giaralis & Petrini, 2017):

$$\nu_{\mathrm{TMDI}} = \frac{\sqrt{1 + 0.5(\beta + \mu)}}{1 + \beta + \mu} \tag{49}$$

$$\xi_{\mathrm{TMDI}} = \sqrt{\frac{(\beta + \mu)[1 + 0.75(\beta + \mu)]}{4(1 + \beta + \mu)[1 + 0.5(\beta + \mu)]}} \tag{50}$$

Equations (49) and (50) are not valid optimization formulas for a TMDI connected to a different story. However, since the objective of this section is solely to assess the effect of mass ratio and damping ratio, the control devices were considered as TMDIs connected in parallel on the same story (see Figure 12), effectively treating them as equivalent TMDs. Under this premise and for the purposes of this section, Equations (49) and (50), which are valid for a classical

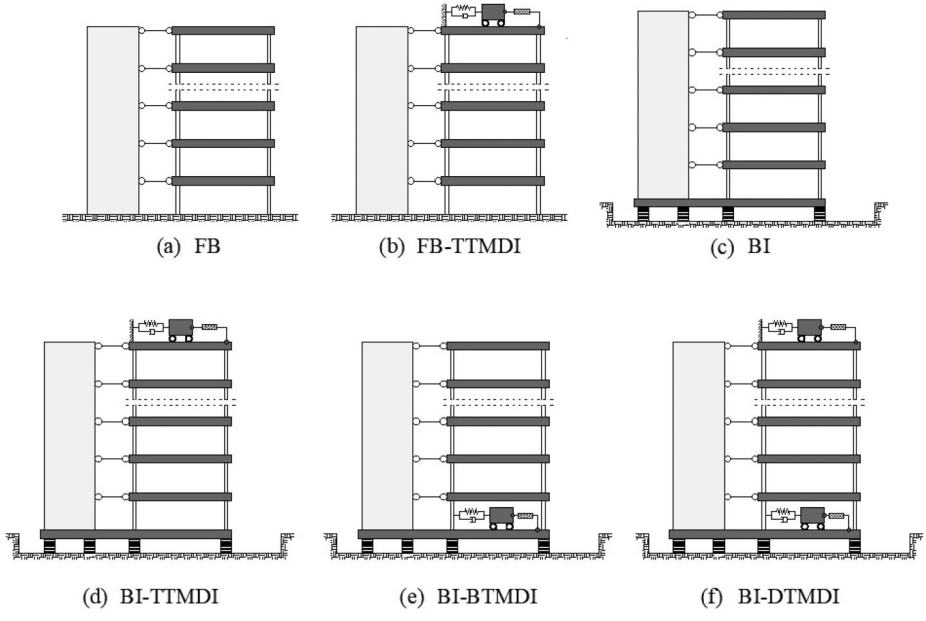

Figure 12. Different building isolator-damper configurations.

Table 7. Dynamic properties of the dampers: B (bottom), T (top).

			TMD ($\beta = 0$, $\mu = 0.02$)				TMDI ($\beta = 0.2$, $\mu = 0.02$)			
Case	Direction	m_{SDOF} [Gg]	T_{TMDI}[s]	m_{TMDI}[Gg]	k_{TMDI}[kN/m]	c_{TMDI}[kN s/m]	T_{TMDI}[s]	m_{TMDI}[Gg]	k_{TMDI}[kN/m]	c_{TMDI}[kN s/m]
FB-TTMDI	*xz*	17	3.70	0.3399	977.71	80.93	4.23	3.74	8262	2418
	yz	11.01	3.48	0.2202	718.33	55.83	3.97	2.42	6070.1	1668.1
BI-TTMDI	*xz*	28.70	7.88	0.5740	365.11	64.26	8.99	6.31	3085.3	1920.2
	yz	25.84	7.70	0.5169	344.31	59.22	8.78	5.69	2909.6	1769.4
BI-BTMDI	*xz*	50.66	7.88	1.0132	644.47	113.43	8.99	11.15	5446	3389.4
	yz	47.87	7.70	0.9574	637.76	109.69	8.78	10.53	5389.3	3277.5
BI-DTMDI	*xz* (B)	50.66	7.82	0.5066	327.02	40.55	8.94	10.64	5260.9	3189.9
	xz (T)	28.70	7.82	0.2870	185.27	22.97	8.94	6.03	2980.5	1807.1
	yz (B)	47.89	7.64	0.4787	323.62	39.21	8.73	10.05	5206.2	3084.6
	yz (T)	25.84	7.64	0.2584	174.71	21.17	8.73	5.43	2810.7	1665.3

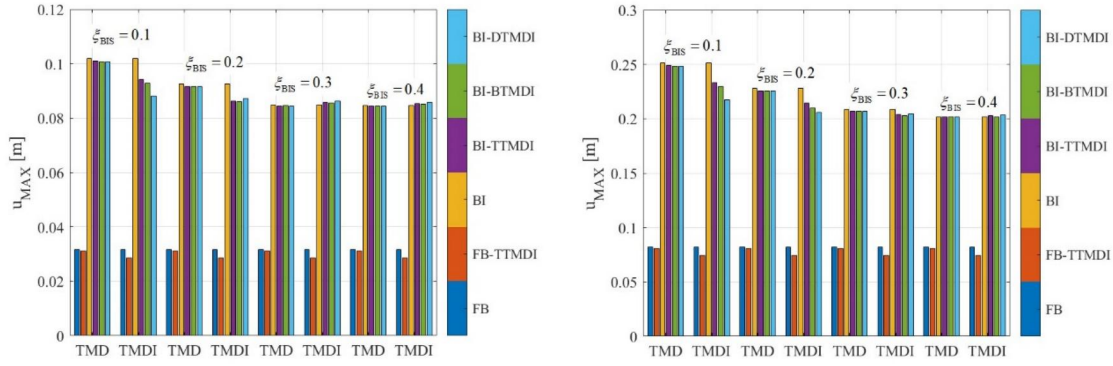

Figure 13. Total peak top floor displacement of the benchmark building: along-wind direction.

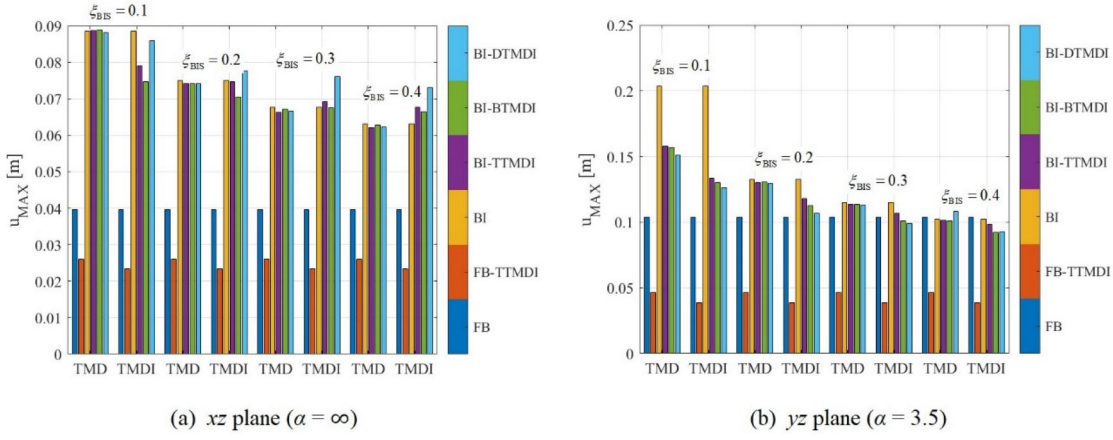

Figure 14. Total peak top floor displacement of the benchmark building: across-wind direction.

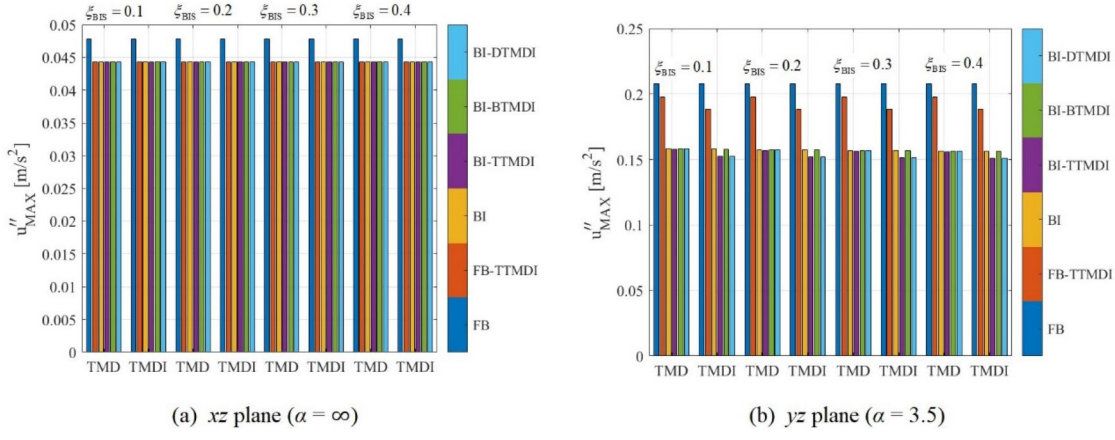

Figure 15. Total peak top floor acceleration of the benchmark building: along-wind direction.

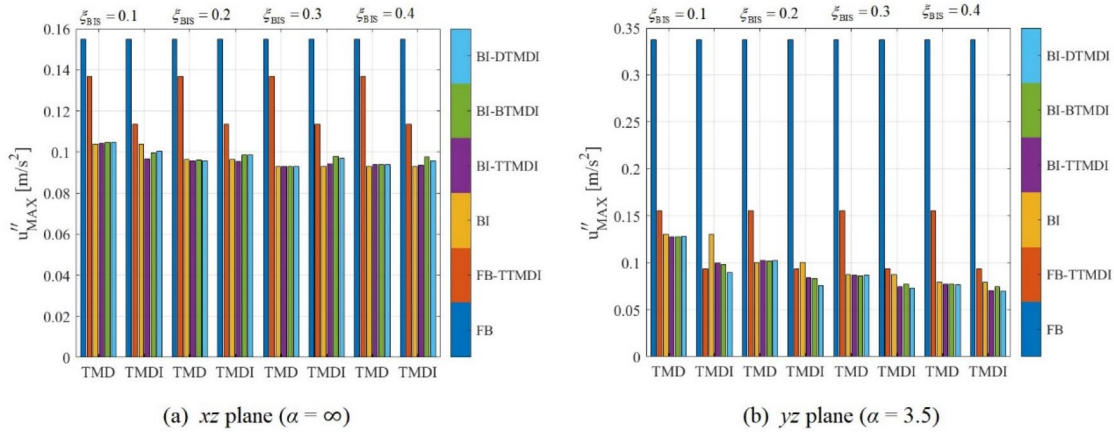

Figure 16. Total peak top floor acceleration of the benchmark building: across-wind direction.

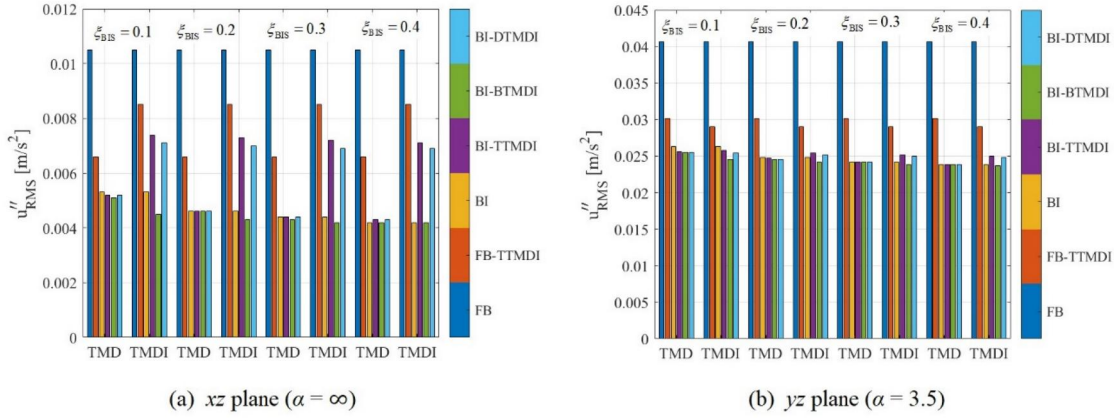

Figure 17. Total RMS top floor acceleration of the benchmark building: along-wind direction.

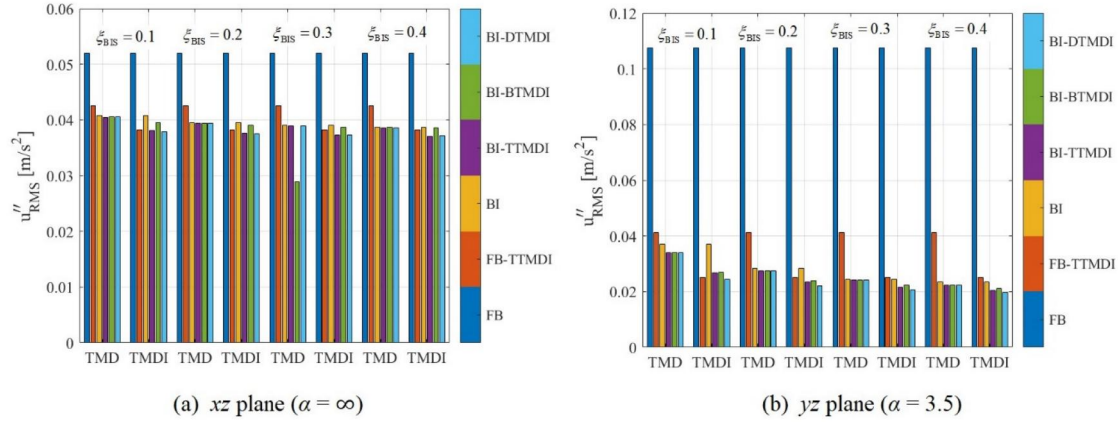

Figure 18. Total RMS top floor acceleration of the benchmark building: across-wind direction.

TMD, allow for a reduction in computational cost. Based on Equations (49) and (50), $\nu_{TMDI} = 0.99$ and $\nu_{TMDI} = 0.86$ for the TMD ($\beta = 0$) and TMDI ($\beta = 0.2$), respectively; whereas $\xi_{TMDI} = 0.0702$ and $\xi_{TMDI} = 0.2175$ for the TMD ($\beta = 0$) and TMDI ($\beta = 0.2$), respectively. In this regard, the expressions in Equations (49) and (50) do not any means achieve optimum TMDI designs for the adopted primary structure against any particular optimization criterion. However, they do yield reasonable values for the stiffness and the damping properties of the TMDI, accounting for the mass-amplification effect of the inerter (Giaralis & Petrini, 2017). Accordingly, the mass, spring stiffness and damping coefficient of the TMDI is shown in Table 7 for the configurations shown in Figure 12. For the specific case of BI-DTMDI, the dynamic properties of the total equivalent TMDI were divided into 2 equal parts for each device (top and bottom) in order to be able to make a realistic comparison between the BI-TTMDI, BI-BTMDI and BI-DTMDI configurations, that is, $\mu = 0.01$ for each device of the BI-DTMDI configuration.

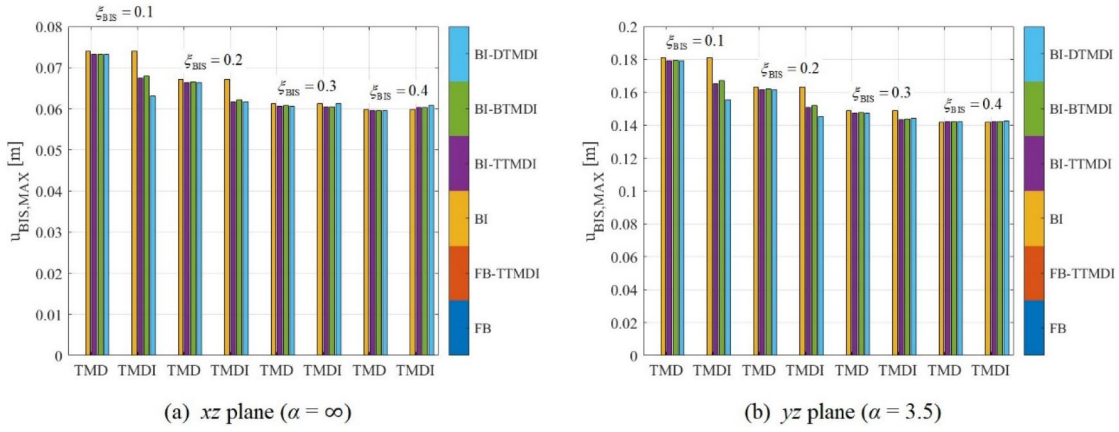

Figure 19. Peak displacement of the base isolator: along-wind direction.

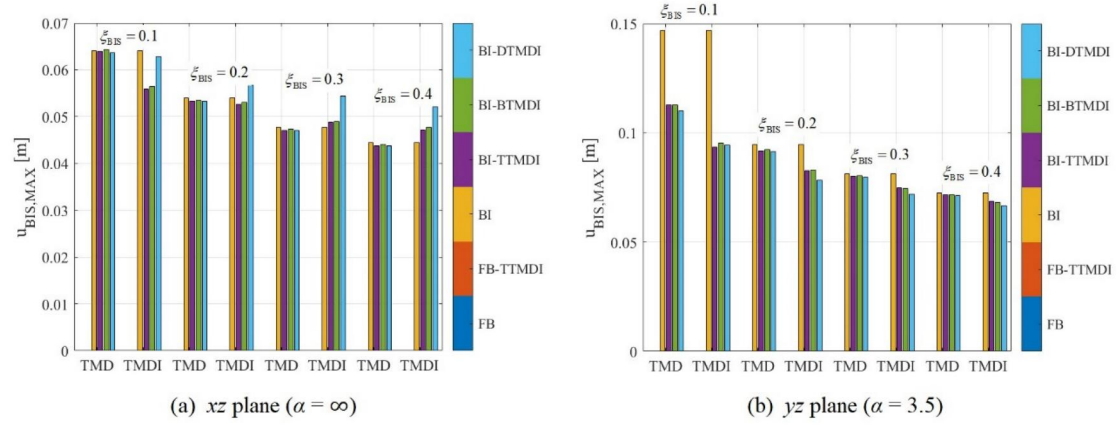

Figure 20. Peak displacement of the base isolator: across-wind direction.

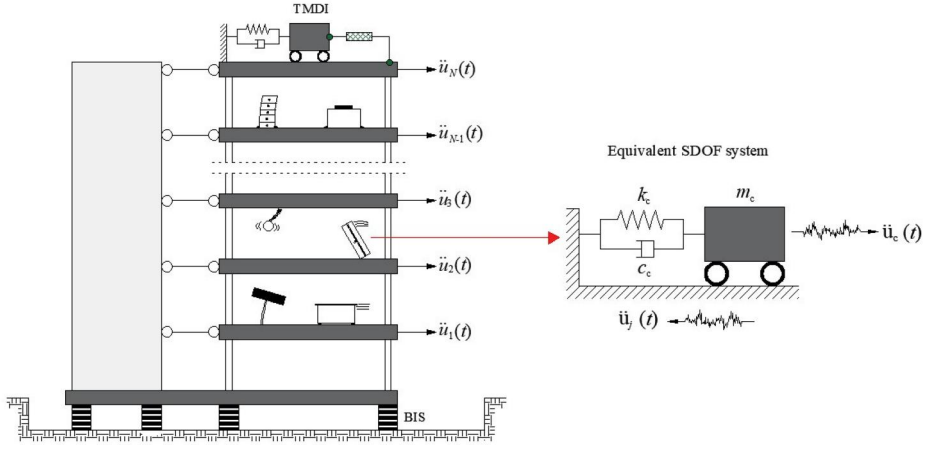

Figure 21. Sketch of the wind-induced vibration for content design.

For wind engineering applications, the total modal damping ratio of a high-rise building is composed by the structural damping ratio plus the aerodynamic damping ratio, which arises from the interaction between the oscillating structure and the wind flowing around it. According to Huergo et al. (2024), the total damping ratio of the benchmark building for both the first and second mode of vibration is approximately equal to 0.01. Accordingly, Figures 13–18 show the total top floor response (base isolator + relative response) of the benchmark building under along-wind and across-wind loads (see Figure 11) considering the six different isolator-damper configurations for both TMD and TMDI; whereas Figures 19 and 20 show the peak displacement of the base isolator under the same conditions.

As already mentioned above, a low damping BIS reduces the peak total displacement of the benchmark building under seismic loads, however, the opposite effect is observed

Table 8. Approximate dynamic properties of contents.

Furniture item	Period of vibration [s]	Damping ratio
Small equipment (computers, printers)	0.05 – 0.2	0.01 – 0.03
Lightweight furniture (chairs, small tables)	0.05 – 0.3	0.02 – 0.04
Medium filing cabinets	0.2 – 0.4	0.03 – 0.05
Heavy furniture (shelves, bookcases)	0.3 – 0.5	0.03 – 0.06
Sensitive laboratory equipment	0.2 – 1	0.01 – 0.04
Medium machinery (small generators)	0.5 – 1.5	0.03 – 0.07
Medium HVAC systems (air conditioners)	0.5 – 1	0.03 – 0.06
Small storage tanks	0.5 – 2	0.04 – 0.07
Large industrial equipment (turbines, generators)	1.5 – 3	0.05 – 0.1
Large storage tanks	1.5 – 4	0.01 – 0.1
Large suspended systems (ducts, platforms)	2 – 5	0.04 – 0.08
Small hanging lamps	0.2 – 0.5	0.02 – 0.05
Large hanging lamps (chandelier)	1 – 2.5	0.03 – 0.06

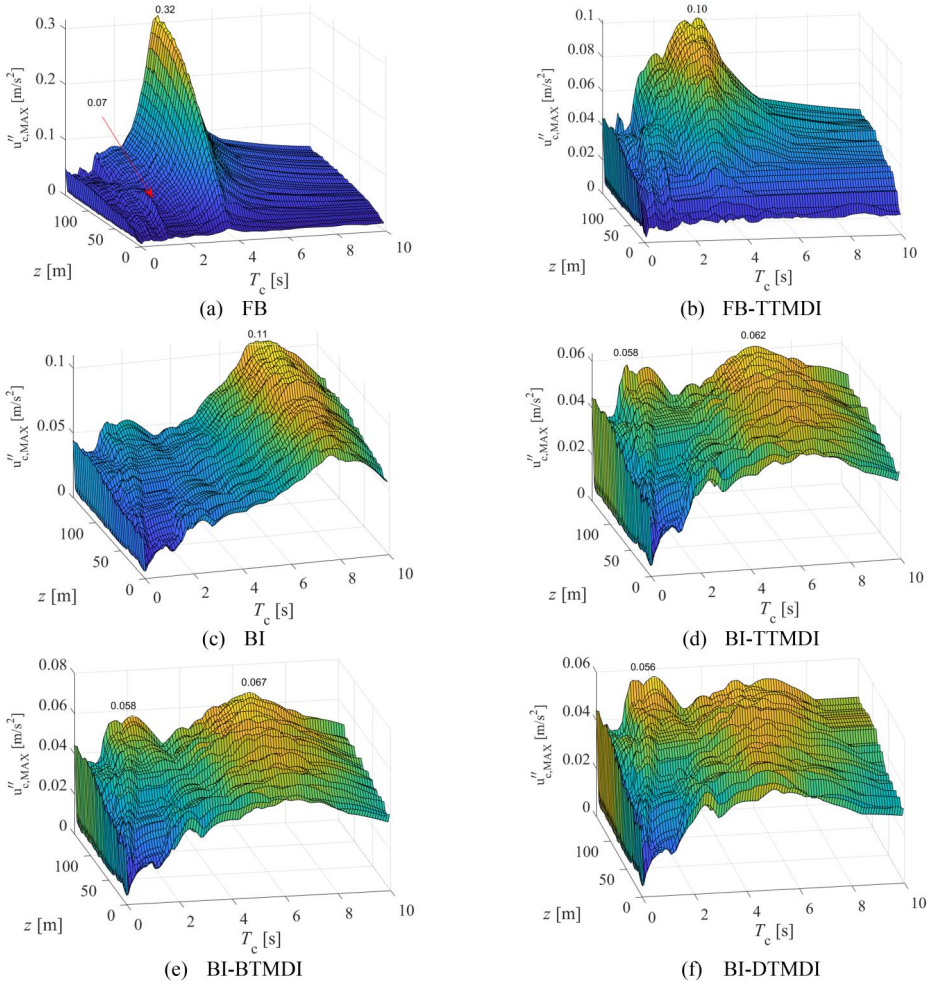

Figure 22. Floor spectra for the along-wind direction: *xz* plane ($\alpha = \infty$).

under lateral wind loads, that is, Figures 13 and 14 show that base isolation of the benchmark building significantly increases both the along-wind and across-wind peak displacements. A low damping BIS ($\xi_{BIS} = 0.1$) increases the along-wind displacements and across-wind displacements in the *xz* plane up to 222% and 123%, respectively; whereas for the *yz* plane these increase up to 207% and 96%, respectively. On the other hand, A high damping BIS ($\xi_{BIS} = 0.4$) increases the along-wind displacements and across-wind displacements in the *xz* plane up to 168% and 59.34%, respectively; whereas for the *yz* plane these increase up to 146% and −1.54%, respectively.

The traditional TMDs ($\beta = 0$) were practically ineffective in controlling along-wind displacements in both planes and across-wind displacements in *xz* plane, on the contrary, they were quite effective in controlling the across-wind peak displacement in the *yz* plane. On the other hand, TMDIs ($\beta = 0.2$) are more effective than TMDs in controlling peak displacements, particularly for the across direction in *yz* plane where TMDIs decreases the response of the base

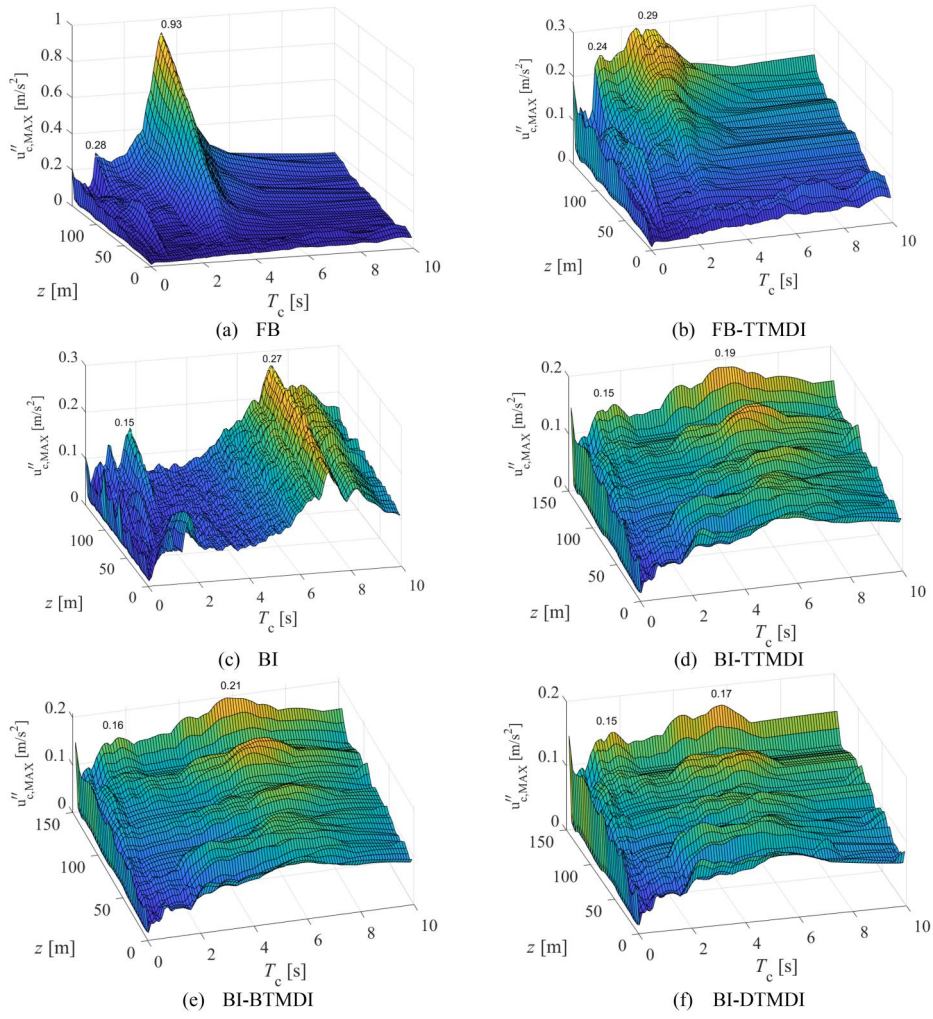

Figure 23. Floor spectra for the along-wind direction: *yz* plane ($\alpha = 3.5$).

isolated building up to 34.32% in comparison with a reduction of 22.51% related the traditional TMD. Furthermore, the effectiveness of TMDIs decreases as the base isolator damping increases.

Based on Figures 15 and 16, the most critical case for peak accelerations is the FB case, however, a single BIS without TMDIs is effective enough to control the response up to 40.05% and 76.43% for *xz* plane and *yz* plane, respectively. In this way, an increase of the base isolation damping increases the effectiveness to control peak accelerations. On the other hand, all the systems (BIS and TMDIs) are ineffective to control along-wind peak accelerations in the *xz* plane, whereas a TTMDI seems to be the best option for most other cases.

Based on Figures 17 and 18, the most critical case for RMS accelerations is also the FB case, however, a single BIS without TMDIs is effective enough to control the response up to 60% and 78.23% for *xz* plane and *yz* plane, respectively. In this way, an increase of the base isolation damping also increases the effectiveness to control RMS accelerations. On the other hand, TMDIs were effective to control the RMS accelerations only for the *yz* plane under across-wind loads, particularly for the BI-DTMDI case; however, the effectiveness of TMDIs also decreases as the base isolator damping increases, e.g. a DTMDI with a low-damping BIS decreases the across-wind RMS acceleration up to 34.14% compared to base isolated building without TMDI, whereas a DTMDI with a high-damping BIS decreases it up to 15.38%.

Based on Figures 19 and 20, all TMDI configuration are quite effective to control the response of a low-damping base isolator. In this way, the peak displacement of the BIS decreases up to 14.73% and 35.71% for the *xz* plane and *yz* plane, respectively. In addition, all TMDI configuration were quite similar to controlling the damage of the BIS.

3.3.2. Floor spectra for content design

The contents of a building such as furniture and lamps are also susceptible to turning moment due to the accelerations induced by the slabs. For earthquake loads, some of these contents must remain undamaged due to their high cost, e.g. hospital equipment. Under wind loads, the vibrations of the contents are not currently reviewed for engineering purposes, however, Figures 15 and 16 show that peak top floor accelerations are higher for pure bending behavior, particularly for the across-wind direction. Therefore, in this section the total peak wind-induced accelerations of the contents are assessed at all stories by computing floor spectra based on the scheme shown in Figure 21, in which the contents

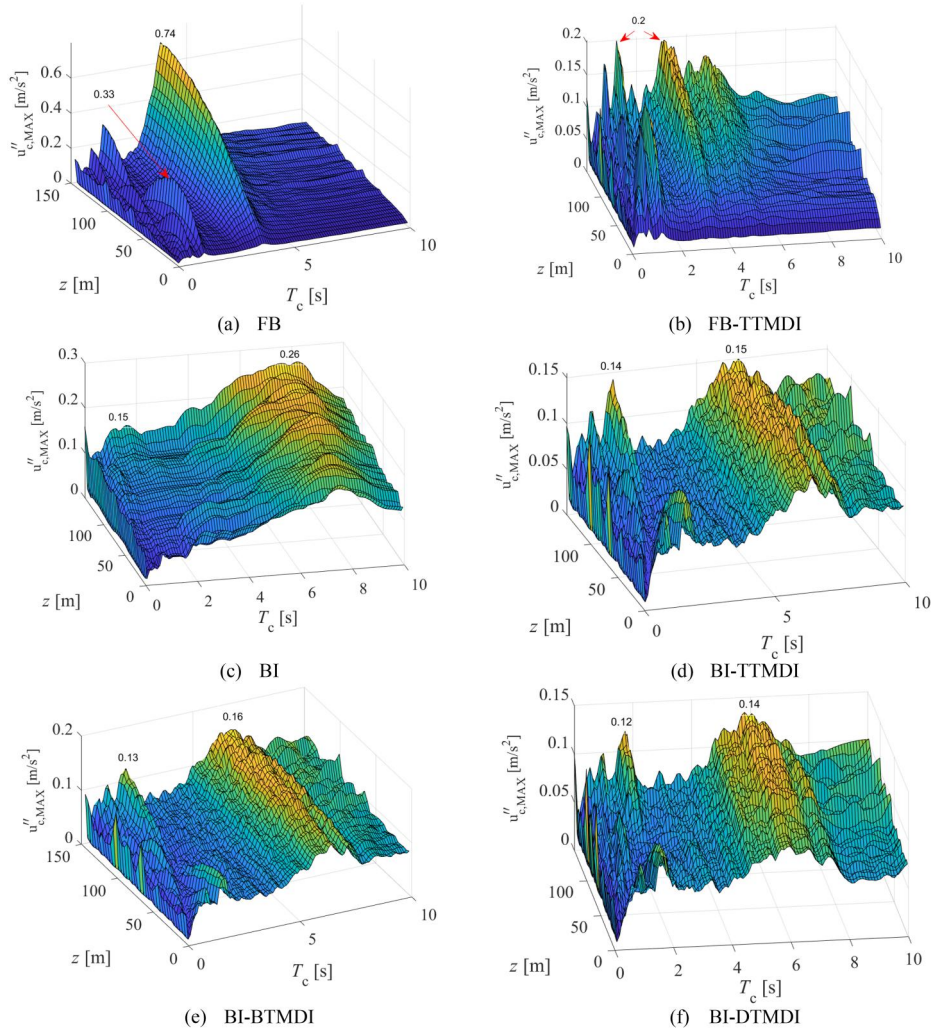

Figure 24. Floor spectra for the across-wind direction: *xz* plane ($\alpha = \infty$).

are idealized as a single degree of freedom system (SDOF) subjected to an acceleration at the base, i.e. the floor acceleration. Accordingly, the acceleration of the content is defined as $\ddot{u}_c(t)$ and its period of vibration is given by:

$$T_c = 2\pi\sqrt{\frac{m_c}{k_c}} \tag{51}$$

where m_c and k_c are the mass and stiffness of the content, respectively. Low-rise furniture will have short vibration periods unless it has a large mass such as industrial equipment. On the other hand, contents such as lamps usually have a high vibration period due to their low stiffness. Regarding the damping of contents, it depends on the material of the furniture, the type of connection and the interaction of the object with the supporting surfaces. Scientific literature (ASCE/SEI 7-10, 2022; Chopra, 2012; Clough & Penzien, 2003; FEMA, 2012; Kazantzi et al., 2020; NTCDS, 2023; Soong & Dargush, 1997; Villaverde, 2009); features some studies on the vibration period and damping ratio of the contents, which are shown in Table 8.

In this way, the floor spectra (see Figures 22–25) were computed for the six cases shown in Figure 12 for the most unfavorable case of damping ratio of the BIS, that is, $\xi_{BIS} =$ 0.1. Based on Table 8, the damping ratio of the floor spectra (content damping) was assumed equal to 0.02.

Based on Figures 22–25, the most critical case occurs for the fixed-base building for contents with periods similar to the building ($T_c \approx 3.5$s) such as large industrial equipment, large storage tanks and large hanging lamps. In the same way as the serviceability limit state, the most unfavorable dynamic response of the contents is related with the lateral resisting systems in pure bending under across-wind loads. In fact, the dynamic response of this type of flexible contents was approximately 9 times greater for the *yz* plane under across-wind loads compared to the *xz* plane under along-wind loads. The response of the contents decreases radically as their location in height decreases, however, for rigid contents with a short vibration period, a second peak of accelerations occurred in the lower floors.

For the FB-TTMDI case, the TTMDI decrease the content acceleration up to 88.81% for the *yz* plane under across-wind loads. However, peak accelerations of contents with a very low vibration period ($T_c < 1$s) are practically the same as those related to the peaks of the spectra ($T_c \approx 3.5$s). On the other hand, the peak accelerations of the contents decrease as their location in height decreases, as occurs in FB case. For the BI case, the base isolators

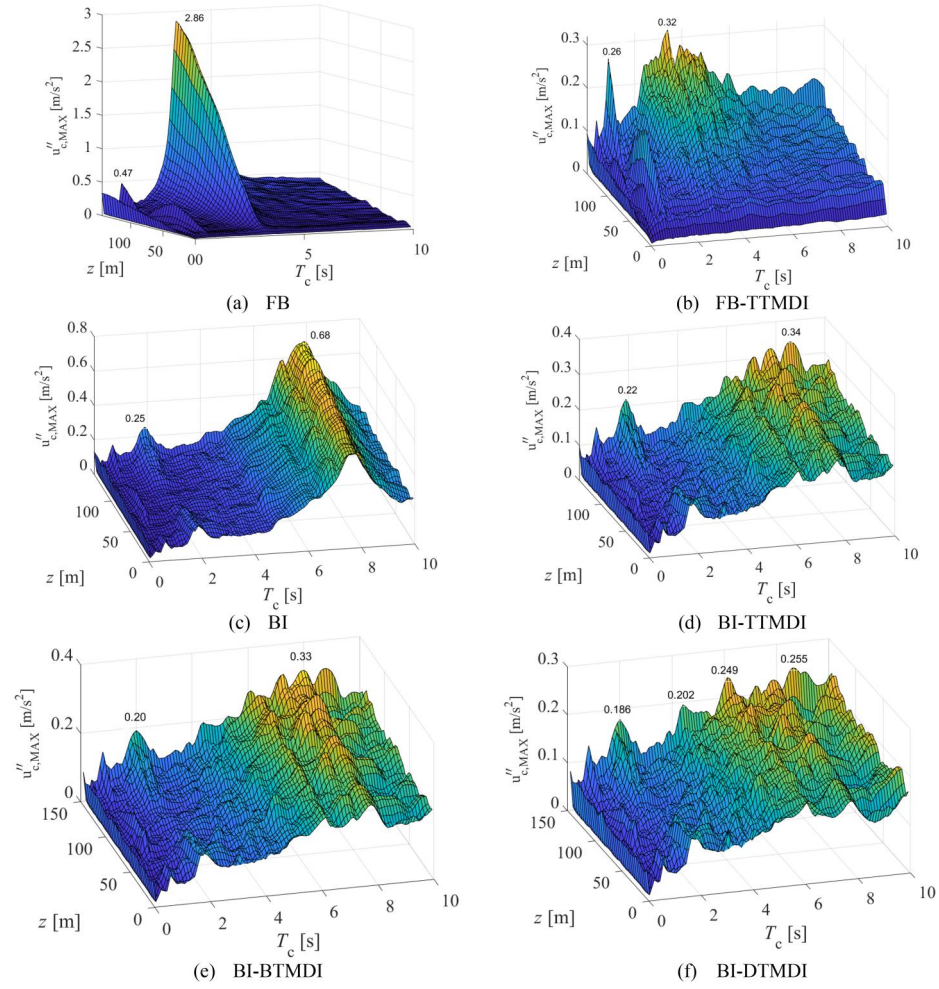

Figure 25. Floor spectra for the across-wind direction: *yz* plane ($\alpha = 3.5$).

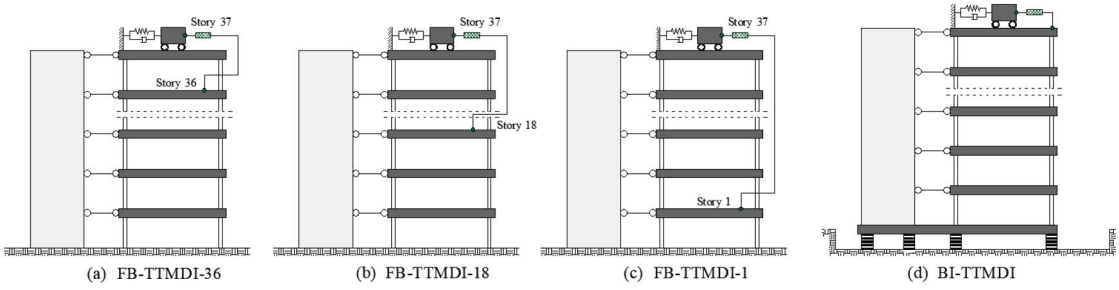

Figure 26. TMDI optimization schemes for the benchmark building ($\mu = \beta = 0.02, \xi_{BIS} = 0.2$).

decrease the content acceleration up to 76.22% for the *yz* plane under across-wind loads. In addition, the peak acceleration is shifted to the period of the isolated building, therefore, the peak acceleration would now occur in extremely flexible contents, thus avoiding the resonance effect for most existing contents ($T_c \approx 8$s). Although the peaks of the spectra are smoother, it is important to note that there is a second peak for rigid contents ($T_c < 2$s). In addition, the maximum accelerations of the contents for the base-isolated buildings are similar in all the stories.

For the base-isolated building with TMDI, the dynamic response of the content decreases between 30 and 50% compared to the BI case, however, the maximum peaks are not smoothed and affect a greater amount of flexible content ($4\text{s} < T_c < 8\text{s}$). On the other hand, the use of TMDI at the bottom slightly decreases the accelerations of the second peak for rigid contents ($T_c < 2$s). It should also be noted that while the maximum peak remains constant for all floors, the second peak increases as the height of the floor increases.

3.3.3. Optimization of tuned mass damper inerter

For fixed-base high-rise buildings under wind loads, the most critical response usually is the acceleration in terms of comfort assessment (serviceability limit state) since seismic loads usually govern the ultimate limit state (check of peak displacement). Since wind-induced accelerations fluctuate over a period of time, the RMS acceleration better reflects

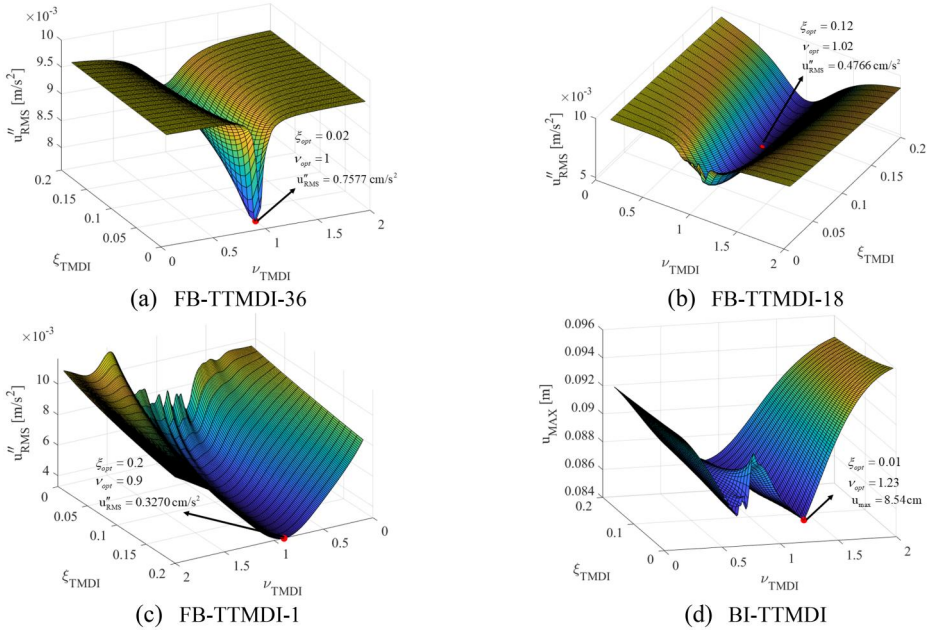

Figure 27. Optimized response for the along-wind direction: *xz* plane ($\alpha = \infty$).

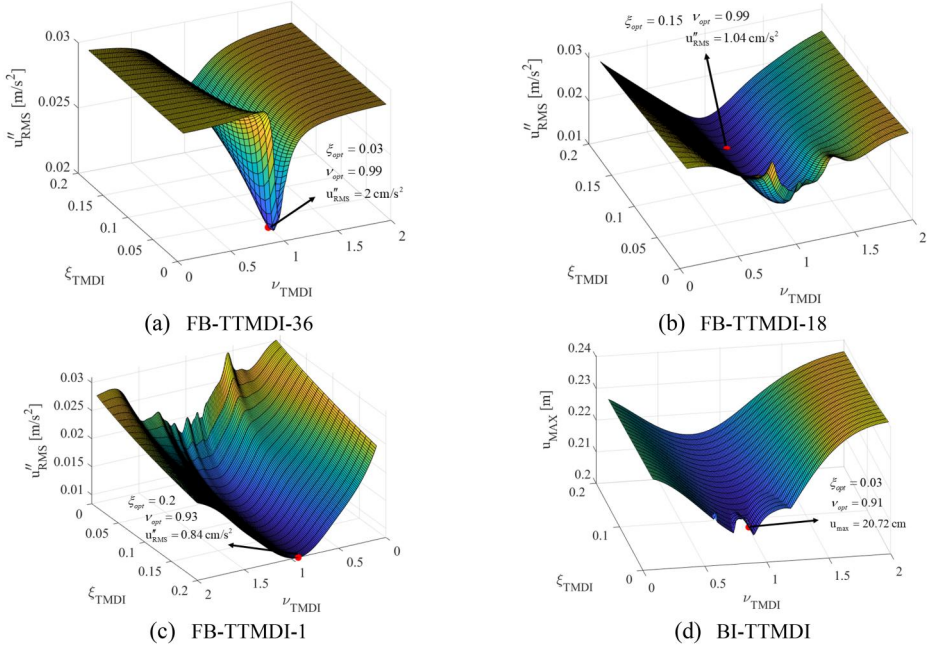

Figure 28. Optimized response for the along-wind direction: *yz* plane ($\alpha = 3.5$).

the total effect of these fluctuations on user comfort instead of peak acceleration. On the other hand, section 3.3.1 showed that total displacements of base-isolated high-rise buildings under wind loads are much greater than the fixed-base cases, therefore, in these circumstances the critical response that must be controlled is the total peak rooftop displacement. For practical purposes, the case of the benchmark building with a top tuned mass damper inerter (TTMDI) will be chosen since it is the most feasible to place due to the free space on the roof and considering that these devices are generally attached at the point of maximum modal amplitude.

Based on the above, the effect of TMDI optimization was assessed for the fixed-base benchmark building considering the effect of connecting the second terminal of the TTMDI to a different story from the one where the device is attached. Consequently, the optimization scheme showed in Figure 26 is proposed for the μ an β values used in sections 3.3.1 and 3.3.2. For each optimization case in Figure 26, the ν_{TMDI} values were ranged from 0 to 2 in increments of 0.01, while ξ_{TMDI} was ranged from 0.01 to 0.2 in increments of 0.01. For the BI-TTMDI case, a value of $\xi_{BIS} = 0.2$ was used to avoid underestimating or overestimating the damping for a base isolator representative of practical professional

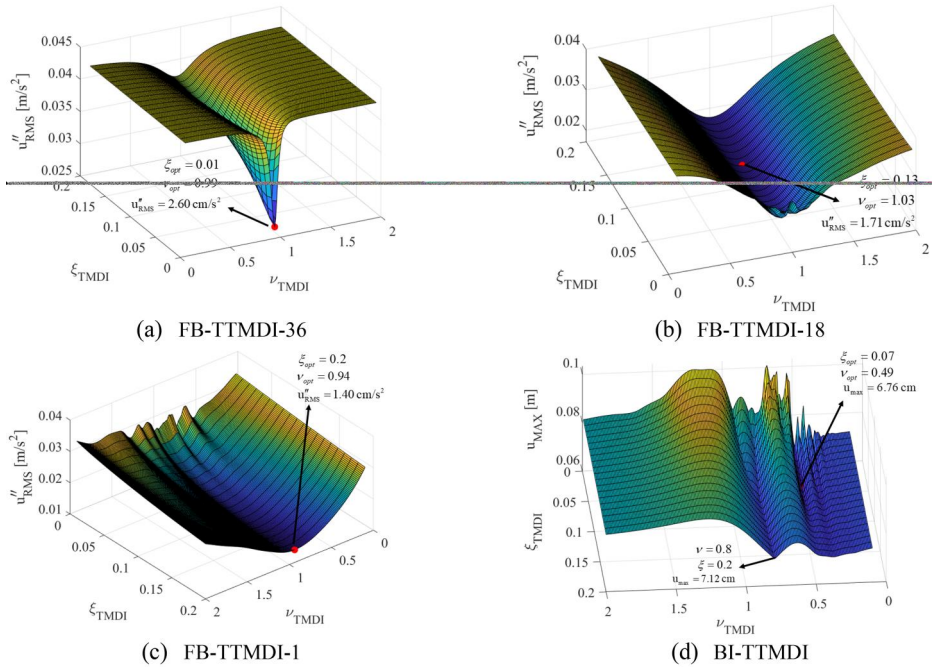

Figure 29. Optimized response for the across-wind direction: *xz* plane ($\alpha = \infty$).

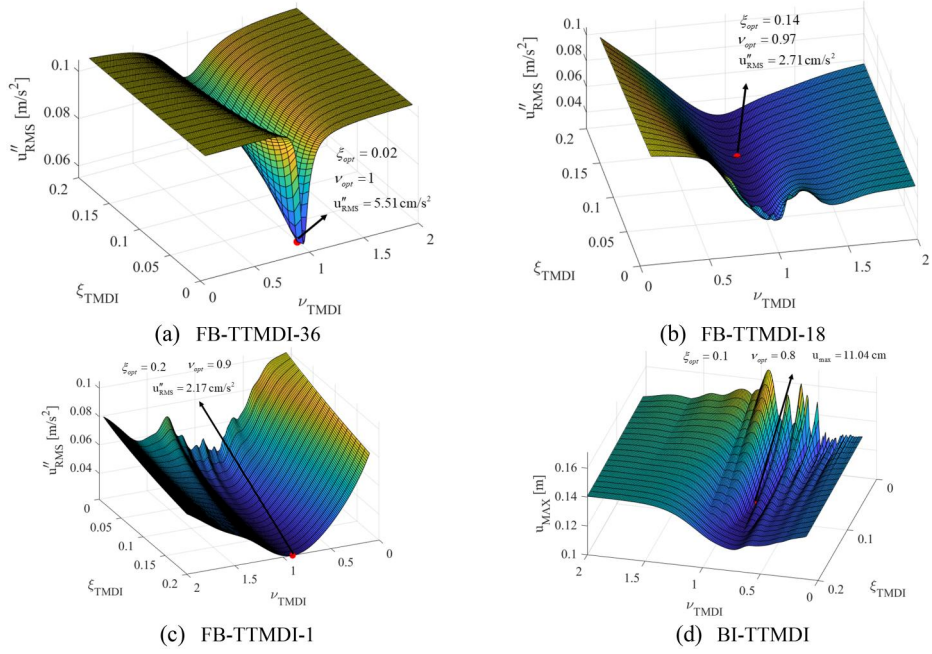

Figure 30. Optimized response for the across-wind direction: *yz* plane ($\alpha = 3.5$).

applications. This means that for a single optimization case, 3820 dynamic time-domain analyses were performed. Accordingly, a total of 61120 dynamic time-domain analyses were conducted considering the along and across-wind loads on both lateral resisting systems of the benchmark building. Therefore, the optimized TMDI parameters to minimize the peak response of the schemes of Figure 26 are shown in Figures 27–30.

Based on Figures 27–30, it can be observed that connecting the TTMDI to a lower story results in greater acceleration reduction compared to a parallel connection at the same story. For the along-wind direction, the FB-TTMDI-1 case reduces the response by 56.84% compared to the FB-TTMDI-36 case in the *xz* plane, while this reduction reaches 58% in the *yz* plane. Moreover, the reduction achieved in the across-wind direction in the *xz* plane is 84.27% when the TTMDI is connected to the 1st story instead of the 36th story. In contrast, a reduction of 60.62% is observed in the *yz* plane for the across-wind direction.

Another noteworthy observation is that, for the FB-TTMDI-36 case, the optimal damping of the TMDI (ξ_{opt}) is small, whereas for the FB-TTMDI-1 case, it is large. Additionally, the ν_{opt} values vary from 0.9 to 1.04 for all fixed-base cases, however, it is observed that one advantage

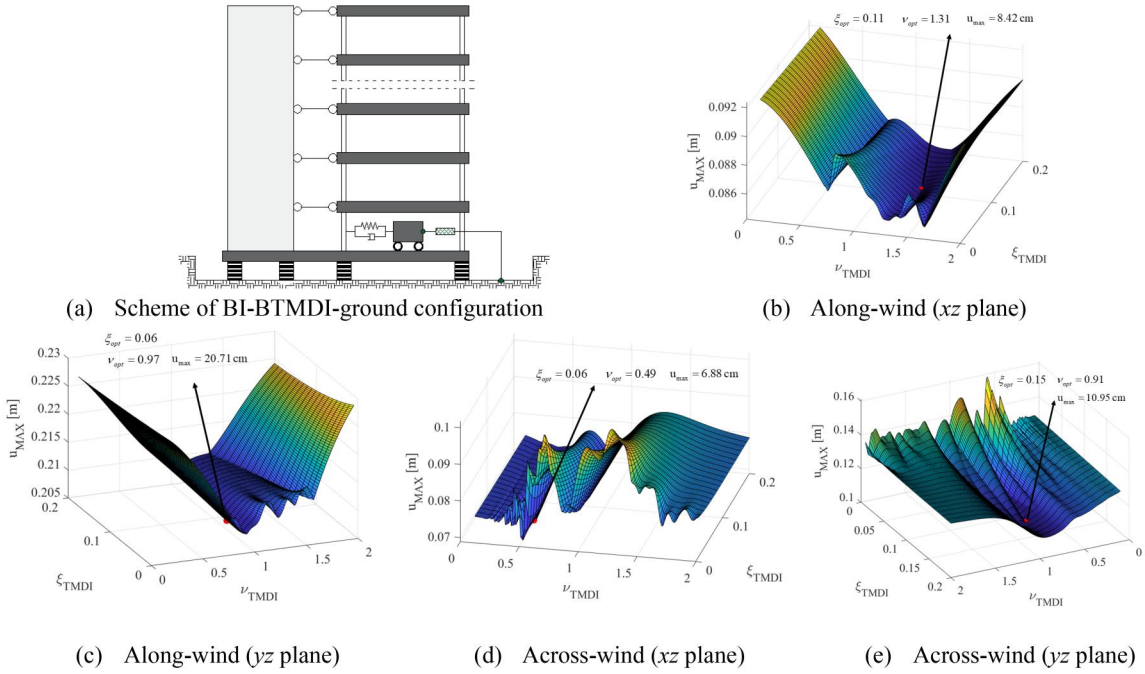

Figure 31. Optimized displacement response for a BI-BTMDI-ground configuration: $(\mu = \beta = 0.02, \xi_{BIS} = 0.2)$.

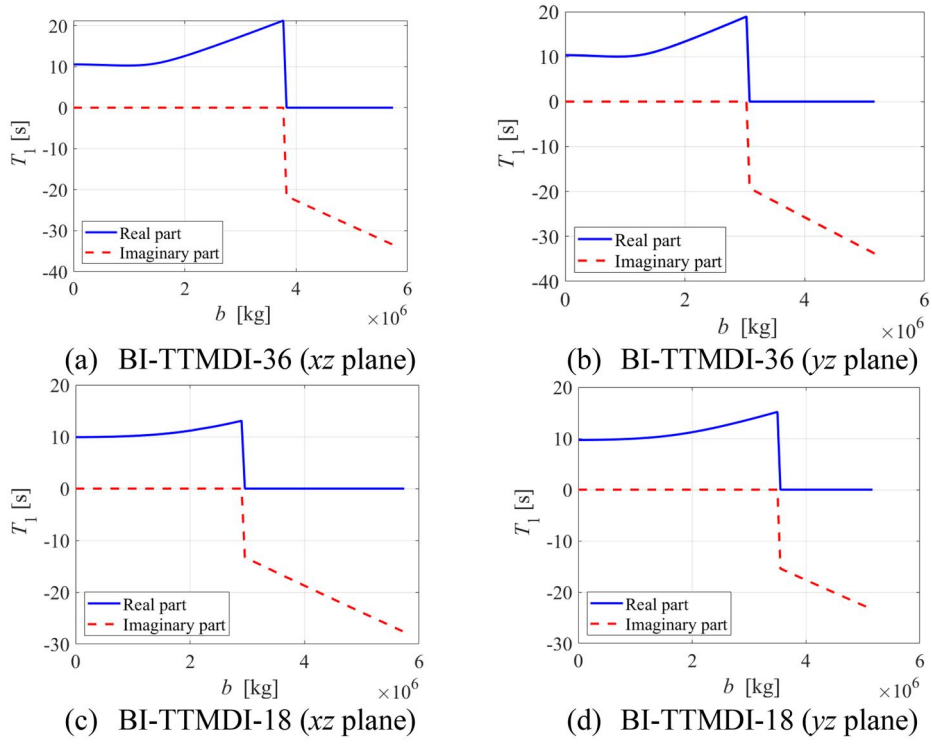

Figure 32. Sensitivity analysis of the inertance coefficient b for a BI-TTMDI-story configuration: $(\mu = \beta = 0.02, \xi_{BIS} = 0.2)$.

of connecting the TMDI to a lower story is the increase in the bandwidth of the optimized response. In other words, the response is reduced not only for values close to ν_{opt}. For the BI-TTMDI case, an optimized TMDI achieves reductions of 1.04% and 3.31% in the total peak rooftop displacement in the along-wind direction for the *xz* and *yz* planes, respectively, compared to a non-optimized TMDI (Equations 49 and 50). Moreover, an optimized TMDI achieves reductions of 9.05% and 6.44% in the across-wind direction for the *xz* and *yz* planes, respectively. For the BI-TTMDI case under along-wind loads, the values of ξ_{opt} are smaller compared to the across-wind direction. Additionally, the ν_{opt} values range from 0.49 to 1.23. In fact, for the *xz* plane, there appear to be two optimization peaks. Another interesting observation is that, for the across-wind direction, there do not appear to be well-defined optimization peaks.

Previous studies on TMDI optimization for base-isolated buildings focus solely on controlling seismic

response. In such cases, the TMDI is typically placed on the base isolator level, which is linked to the ground instead of other stories since the goal is to control the displacements of the base isolator (De Domenico & Ricciardi, 2018; Di Mateo et al., 2019; Masnata et al., 2021). For wind engineering applications, Section 3.3.1 demonstrated the imperative need to control the total displacement of isolated buildings. Therefore, it is of interest to explore the optimization of a bottom TMDI (BTMDI) with its second terminal linked to the ground, as this could enhance the efficiency of the inerter in controlling the sway motion. Consequently, the results of this optimization for a BI-BTMDI-ground configuration are presented in Figure 31, based on 15280 time-domain dynamic analyses.

Figure 31 shows that a BI-BMDI-ground configuration controls the total peak rooftop displacement in the *yz* plane similarly to the BI-TTMDI case. However, the BI-BTMDI-ground configuration achieves a sway motion reduction of up to 5.62% for the *xz* plane in comparison to the BI-TMDI configuration. Based on Equations (15) and (18), the inertial coefficient b depends on the single degree of freedom equivalent mass to be tuned, such that m_{SDOF} increases as α increases. This could explain why the response control in the *xz* plane is greater for the BI-BMDI-ground configuration in comparison to the *yz* plane.

Base isolation already generates long periods without TMDIs (7.76 and 7.59 s for the benchmark building). If the TMDI has a high inertia parameter b and is linked to a different level from its support, it seems that it may alter the system's modal distribution. This may lead to undesired dynamic interactions, reflected in coupled modes with imaginary components in the modal analysis. This type of numerical issue had not been previously reported in scientific literature for fixed-based condition (Hu et al., 2018; Wang & Giaralis, 2021), in fact, as observed in Figures 27–30, configurations FB-TTMDI-36, FB-TTMDI-18 and FB-TTMDI-1 do not produce numerical instabilities regardless of the value of the inertial coefficient b. An innovative structural modification, top-story softening, in conjunction with an optimally tuned TTMDI has been previously studied by Wang and Giaralis (2021) to improve the wind performance of fixed-base buildings, however, the softening of the top floor was achieved by reducing the lateral stiffness of that story facilitating the analysis of the interactions between the TMDI and the stories, as there is no significant decoupling of the structural motion. On the other hand, in our case study, the base isolators decouple the building's motion from the ground, which modifies the system's dynamic response and can affect the interaction with the TMDI differently, especially in terms of modification of the vibration period and the distribution of the vibration modes.

Accordingly, a sensitivity analysis of the inertial coefficient b was conducted for the case of the base-isolated building with a top TMDI linked to stories 36 and 18 (BI-TTMDI-36 and BI-TTMDI-18). In this sensitivity analysis (see Figure 32), it is observed that for small values of b, the previously mentioned instability problem does not occur; however, it begins to appear for large values of b, that is, when the system has an excessively large fundamental period, T_1.

4. Conclusions

This study evaluated the effectiveness of the tuned mass damper inerter (TMDI) in controlling wind-induced vibrations in a base-isolated high-rise building with various lateral resisting systems. Key findings include that hybrid control systems, such as base isolation with TMDI, are effective in reducing displacements and accelerations in areas prone to both earthquakes and extreme wind. A medium-damping base isolation system (BIS) is recommended to balance both types of control, as a low-damping BIS is effective against earthquake-induced damage, and a high-damping BIS better controls wind-induced vibrations.

Lateral resisting systems with higher flexural stiffness, such as shear wall-frame and tubular systems, enhance the effectiveness of TMDIs in controlling base isolator displacements, wind-induced vibrations (especially across-wind), and peak accelerations of building contents when combined with a medium-damping BIS. However, the cost of implementing TMDIs is expected to be higher than that of traditional tuned mass dampers (TMDs), and their use must be justified by the benefits they offer in controlling dynamic response. On the other hand, a BI-DTMDI configuration is slightly more effective than other TMDI configurations, but its cost-benefit ratio may be lower. Therefore, for cost-effective practical applications, placing a single TMDI at the point of maximum modal amplitude (typically at the rooftop level) is more feasible.

For fixed-base buildings, optimizing a top TMDI by connecting it to a lower story enhances its effectiveness by increasing the response bandwidth, thereby improving control across a wider range of frequencies, not just those close to the optimal frequency ratio. However, the cost and complexity of these connections must justify their adoption over the use of traditional top TMDs. In some cases, replacing TMDIs with alternative control devices, such as viscous fluid dampers, may be more feasible. For an optimized top TMDI connected to a different story, it is recommended to use a low-damping TMDI for connections to upper stories, and a high-damping TMDI for connections to lower stories.

In addition, for base-isolated buildings with a top TMDI linked to a different story, it is recommended to connect the TMDI at the same level to avoid undesirable dynamic interactions, or alternatively, use traditional TMDs at different locations if it does not substantially increase costs.

Further studies should explore additional TMDI configurations and their optimization for different wind load conditions. The impact of various base isolation systems and the effect of alternative control devices on building response should also be investigated in future research.

Acknowledgments

The support received from Universidad de Monterrey for this research is gratefully acknowledged. The third author participated in this research as Global Community Professor at Universidad de Monterrey.

Disclosure statement

No potential conflict of interest was reported by the author(s).

Data availability

Data will be made available on request.

References

ASCE/SEI 7-10. (2022). *Minimum design loads for buildings and other structures*.

Bachmann, H., Ammann, W. J., Deischl, F., Eisenmann, J., Floegl, I., Hirsch, G. H., Klein, G. K., Lande, G. J., Mahrenholtz, O., Natke, H. G., Nussbaumer, H., Pretlove, A. J., Rainer, J. H., Saemann, E. U., & Steinbeisser, L. (1995). *Vibration problems in structures: Practical guidelines* (2nd ed.). Birkhäuser.

Becker, T. C., Yamamoto, S., Hamaguchi, H., Higashino, M., & Nakashima, M. (2015). Application of isolation to high-rise buildings: A Japanese design case study through a U.S. design code lens. *Earthquake Spectra*, *31*(3), 1451–1470. https://doi.org/10.1193/052813EQS136M

Boardman, P. R., Wood, B. J., & Carr, A. J. (1983). Union House – A cross braced structure with energy dissipators. *Bulletin of the New Zealand Society for Earthquake Engineering*, *16*(2), 83–97. https://doi.org/10.5459/bnzsee.16.2.83-97

CFE. (2020). *Manual de Diseño de Obras Civiles: Diseño por viento*. Instituto de Investigaciones Eléctricas.

Chopra, A. K. (2012). *Dynamics of structures: Theory and applications to earthquake engineering* (4th ed.). Prentice Hall.

Clough, R. W., & Penzien, J. (2003). *Dynamics of structures* (3rd ed.). Computers & Structures, Inc.

Dai, J., Xu, Z. D., & Gai, P. P. (2019). Tuned mass-damper-inerter control of wind-induced vibration of flexible structures based on inerter location. *Engineering Structures*, *199*, 109585. https://doi.org/10.1016/j.engstruct.2019.109585

Das, A., Banerjee, A., Sahoo, D. R., & Matsagar, V. (2024). Inerter-based tuned mass dampers for response control of multi-degree-of-freedom structures subjected to wind and earthquake excitations. *Structure and Infrastructure Engineering*, 1–14. https://doi.org/10.1080/15732479.2024.2345280

Davenport, A. G. (1962). The response of slender line-like structures to a gusty Wind. *Proceedings - Institution of Civil Engineers*, *23*(3), 389–408. https://doi.org/10.1680/iicep.1962.10876

De Domenico, D., & Ricciardi, G. (2018). Optimal design and seismic performance of tuned mass damper inerter (TMDI) for structures with nonlinear base isolation systems. *Earthquake Engineering & Structural Dynamics*, *47*(12), 2539–2560. https://doi.org/10.1002/eqe.3098

Di Matteo, A., Masnata, C., & Pirrotta, A. (2019). Simplified analytical solution for the optimal design of tuned mass damper inerter for base isolated structures. *Mechanical Systems and Signal Processing*, *134*, 106337. https://doi.org/10.1016/j.ymssp.2019.106337

Elsesser, E., Honeck, W., & Walters, M. (1995). Seismic retrofit of the Oakland City Hall, Oakland, California. *Structural Engineering International*, *5*(1), 12–14. https://doi.org/10.2749/101686695780601448

ESDU. (2001). Characteristic of atmospheric turbulence near the ground, part II: Single point data for strong winds (neutral atmosphere). *Technical Reports Series* (Vol. 85020).

Federal Emergency Management Agency (FEMA). (2012). *Reducing the risks of nonstructural earthquake damage* (FEMA E-74).

Gao, Y., Wu, Y., Li, D., Liu, H., & Zhang, N. (2012). An improved approximation for the spectral representation method in the simulation of spatially varying ground motions. *Probabilistic Engineering Mechanics*, *29*, 7–15. https://doi.org/10.1016/j.probengmech.2011.12.001

Giaralis, A., & Petrini, F. (2017). Wind-induced vibration mitigation in tall buildings using the tuned mass-damper-inerter. *Journal of Structural Engineering*, *143*(9), 1–11. https://doi.org/10.1061/(ASCE)ST.1943-541X.0001863

Harris, R. I., & Deaves, D. M. (1981). The structure of strong winds. *Wind Engineering in the Eighties: Proceedings of the CIRIA Conference, Construction Industry Research and Information Association*. https://cir.nii.ac.jp/crid/1570854174978636928

Hu, Y., Chen, M. Z. Q., & Smith, M. C. (2018). Natural frequency assignment for mass-chain systems with inerters. *Mechanical Systems and Signal Processing*, *108*, 126–139. https://doi.org/10.1016/j.ymssp.2018.01.038

Huergo, I. F., & Hernández, H. (2019). Coupled shear-flexural model for dynamic analysis of fixed-base tall buildings with tuned mass dampers. *The Structural Design of Tall and Special Buildings*, *28*(17), e1671. https://doi.org/10.1002/tal.1671

Huergo, I. F., & Hernández, H. (2020). Coupled-two-beam model for dynamic analysis of tall buildings with tuned mass dampers including soil-structure interaction. *Struct. Design Tall Spec. Build*, *29*(1), e1683. https://doi.org/10.1002/tal.1683

Huergo, I. F., Hernández-Barrios, H., & Gómez-Martíne, R. (2022). Analytical simulation of 3D-wind induced vibrations of rectangular tall buildings in time domain. *Shock and Vibration*, *2022*, 1–26. https://doi.org/10.1155/2022/7283610

Huergo, I. F., Hernández-Barrios, H., & Gómez-Martínez, R. (2024). Along and across-wind vibration control of shear wall-frame buildings with flexible base by using passive dynamic absorbers. *Wind and Structures*, *38*(1), 15–42. https://doi.org/10.12989/was.2024.38.1.015

Huergo, I. F., Hernández-Barrios, H., & Patlán, C. M. (2020). A continuous-discrete approach for pre-design of flexible-base tall buildings with fluid viscous dampers. *Soil Dynamics and Earthquake Engineering*, *131*, 106042. https://doi.org/10.1016/j.soildyn.2020.106042

Huergo, I. F. (2021). *Control pasivo de vibraciones inducidas por viento en edificios altos con base flexible* [Doctoral Dissertation]. Universidad Nacional Autónoma de México. http://132.248.9.195/ptd2021/febrero/0808340/Index.html

Jangid, R. S., & Datta, T. K. (1995). Seismic behavior of base-isolated buildings: A state-of-the-art review. *Proceedings of the Institution of Civil Engineers–Structures and Buildings*, *110*(2), 186–203. https://doi.org/10.1680/istbu.1995.27599

Jayachandran, P. (2009). *Design of tall buildings-preliminary design and optimization* [Paper presentation]. National Workshop on High-Rise and Tall Buildings, University of Hyderabad, Hyderabad, India.

Kareem, A. (1997). Modelling of base-isolated buildings with passive dampers under wind. *Journal of Wind Engineering and Industrial Aerodynamics*, *72*, 323–333. https://doi.org/10.1016/S0167-6105(97)00232-8

Kazantzi, A. K., Vamvatsikos, D., & Miranda, E. (2020). Evaluation of seismic acceleration demands on building nonstructural elements. *Journal of Structural Engineering*, *146*(7), 04020118. https://doi.org/10.1061/(ASCE)ST.1943-541X.0002676

Kelly, J. M. (1999). The role of damping in seismic isolation. *Earthquake Engineering & Structural Dynamics*, *28*(1), 3–20. https://doi.org/10.1002/(SICI)1096-9845(199901)28:1%3C3::AID-EQE801%3E3.0.CO;2-D

Komuro, T., Nishikawa, Y., Kimura, Y., & Isshiki, Y. (2005). Development and realization of base isolation system for high-rise buildings. *Journal of Advanced Concrete Technology*, *3*(2), 233–239. https://doi.org/10.3151/jact.3.233

Krenk, S. (1996). Wind field coherence and dynamic wind forces. *IUTAM Symposium on Advances in Nonlinear Stochastic Mechanics*, 47, 269–278. https://link.springer.com/chapter/10.1007/978-94-009-0321-0_25

Lagos, R., Boroschek, R., Retamales, R., & Lafontaine, M. (2014). Seismic isolation of the Nunoa Capital Building, the tallest base isolated residential building in The Americas. Tenth U.S. National Conference on Earthquake Engineering. *Frontiers of Earthquake Engineering*.

Liang, B., Shishu, X., & Jiaxiang, T. (2002). Wind effects on habitability of base-isolated buildings. *Journal of Wind Engineering and Industrial Aerodynamics*, *90*(12-15), 1951–1958. https://doi.org/10.1016/S0167-6105(02)00300-8

Liang, S., Liu, S., Li, Q. S., Zhang, L., & Gu, M. (2002). Mathematical model of acrosswind dynamic loads on rectangular tall buildings. *Journal of Wind Engineering and Industrial Aerodynamics*, *90*(12-15), 1757–1770. (). https://doi.org/10.1016/S0167-6105(02)00285-4

Li, Z., Chen, X., Huang, G., Yang, Q., Zhou, X., & Pang, H. (2023). Coupled dynamic analysis of tall buildings isolated with friction pendulum bearings under three-dimensional wind loads. *Journal of Wind Engineering and Industrial Aerodynamics*, *234*, 105332. https://doi.org/10.1016/j.jweia.2023.105332

Li, Z., Huang, G., Chen, X., Zhou, Y., & Yang, Q. (2020). Wind-resistant design and equivalent static wind load of base-isolated tall building: A case study. *Engineering Structures*, *212*, 110533. https://doi.org/10.1016/j.engstruct.2020.110533

Masnata, C., Di Matteo, A., Adam, C., & Pirrotta, A. (2021). Assessment of the tuned mass damper inerter for seismic response control of base-isolated structures. *Structural Control and Health Monitoring*, *28*(2), 1–17. https://doi.org/10.1002/stc.2665

Matsagar, V. A., & Jangid, R. S. (2004). Influence of isolator characteristics on the response of base-isolated structures. *Engineering Structures*, *26*(12), 1735–1749. https://doi.org/10.1016/j.engstruct.2004.06.011

Miranda, E., & Reyes, C. J. (2002). Approximate lateral drift demands in multistory buildings with nonuniform stiffness. *Journal of Structural Engineering*, *128*(7), 840–849. https://doi.org/10.1061/(ASCE)0733-9445(2002)128:7(840)

Miranda, E., & Taghavi, S. (2005). Approximate floor acceleration demands in multistory buildings. I.: Formulation. *Journal of Structural Engineering*, *131*(2), 203–211. https://doi.org/10.1061/(ASCE)0733-9445(2005)131:2(203)

Mostaghel, N., & Khodaverdian, M. (1987). Dynamics of resilient-friction base isolator. *Earthquake Engineering & Structural Dynamics*, *15*(3), 379–390. https://doi.org/10.1002/eqe.4290150307

Naeim, F., & Kelly, J. M. (1999). *Design of seismic isolated structures: From theory to practice*. John Wiley & Sons.

Nakagawa, K., Shimazaki, D., Yoshida, S., & Okada, K. (2015). Application of seismic isolation systems in Japanese high-rise buildings. *CTBUH Journal*, 2, 36–40.

NTCDS. (2023). *Normas Técnicas Complementarias para Diseño por Sismo*. Gaceta Oficial de la Ciudad de México.

Pang, H., Yang, Q., Liu, M., Hui, Y., & Cheng, B. (2022). The influence of wind direction on the inelastic responses of a base-isolated square section high-rise building. *Buildings*, *12*(8), 1208. https://doi.org/10.3390/buildings12081208

Petrini, F., Giaralis, A., & Wang, Z. (2020). Optimal tuned mass-damper-inerter (TMDI) design in wind-excited tall buildings for occupants′ comfort serviceability performance and energy harvesting. *Engineering Structures*, *204*, 109904. https://doi.org/10.1016/j.engstruct.2019.109904

Quan, Y., Zhao, W., & Qiao, H. (2023). Improved model for parametric optimization of tuned mass damper-inerter for wind-induced vibration control of high-rise building. *Structures*, *56*, 104862. https://doi.org/10.1016/j.istruc.2023.07.052

Saha, S. K., Matsagar, V. A., & Gupta, A. (2015). *Wind response of base-isolated building* [Paper presentation]. 14th International Conference on Wind Engineering, Porto Alegre, Brazil.

Saiful, A. B. M., Jameel, M., Uddin, M. A., & Ishtiaq, S. (2011). Simplified design guideline for seismic base isolation in multi-storey buildings for Bangladesh National Building Code (BNBC). *International Journal of Physical Sciences*, *6*(23), 5467–5486. https://doi.org/10.5897/IJPS11.795

Shinozuka, M., Yun, C. B., & Seya, H. (1990). Stochastic methods in wind engineering. *Journal of Wind Engineering and Industrial Aerodynamics*, *36*(2), 829–843. https://doi.org/10.1016/0167-6105(90)90080-V

Smith, M. C. (2002). Synthesis of mechanical networks: The inerter. *IEEE Transactions on Automatic Control*, *47*(10), 1648–1662. https://doi.org/10.1109/TAC.2002.803532

Soong, T. T., & Dargush, G. F. (1997). *Passive energy dissipation systems in structural engineering*. John Wiley & Sons.

Stanikzai, M. H., Elias, S., & Rupakhety, R. (2020). Seismic response mitigation of base-isolated buildings. *Applied Sciences*, *10*(4), 1230. https://doi.org/10.3390/app10041230

Steyer, M. A. (2002). *Multifunctionality of distributed sloshing dampers in buildings* [Master′s thesis]. Massachusetts Institute of Technology. http://hdl.handle.net/1721.1/84834

Su, N., Peng, S., Hong, N., & Xia, Y. (2022). Wind-induced vibration absorption using inerter-based double tuned mass dampers on slender structures. *Journal of Building Engineering*, *58*, 104993. https://doi.org/10.1016/j.jobe.2022.104993

Taniguchi, T., Der Kiureghian, A., & Melkumyan, M. (2008). Effect of tuned mass damper on displacement demand of base-isolated structures. *Engineering Structures*, *30*(12), 3478–3488. https://doi.org/10.1016/j.engstruct.2008.05.027

Tian, J., & Chen, X. (2023). 3D coupled wind-induced inelastic response of base-isolated tall buildings with eccentricity and biaxial interaction of hysteretic restoring base forces. *Journal of Wind Engineering and Industrial Aerodynamics*, *232*, 105252. https://doi.org/10.1016/j.jweia.2022.105252

Tsai, H. C. (1995). The effect of tuned-mass dampers on the seismic response of base-isolated structures. *International Journal of Solids and Structures*, *32*(8-9), 1195–1210. https://doi.org/10.1016/0020-7683(94)00150-U

Vickery, B. J. (1968). Load fluctuations in turbulent flow. *Journal of the Engineering Mechanics Division*, *94*(1), 31–46. https://doi.org/10.1061/JMCEA3.0000941

Villaverde, R. (2009). *Seismic design of secondary structures and non-structural components*. CRC Press.

Wang, Z., & Giaralis, A. (2021). Top-story softening for enhanced mitigation of vortex shedding-induced vibrations in wind-excited tuned mass damper inerter-equipped tall buildings. *Journal of Structural Engineering*, *147*(1), 1–16. https://doi.org/10.1061/(ASCE)ST.1943-541X.0002838

Wu, X., Huang, J., Yan, G., Yan, X., & Lü, J. (2016). Optimization of isolation structure under wind load excitation and experimental study of the wind resistant bearing. *Journal of Shanghai Jiaotong University (Science)*, *21*(6), 719–728. https://doi.org/10.1007/s12204-016-1786-0

Xiang, P., & Nishitani, A. (2014). Optimum design for more effective tuned mass damper system and its application to base-isolated buildings. *Structural Control and Health Monitoring*, *21*(1), 98–114. https://doi.org/10.1002/stc.1556

Yang, J. N., Danielians, A., & Liu, S. C. (1991). Aseismic hybrid control systems for building structures. *Journal of Engineering Mechanics*, *117*(4), 836–853. https://doi.org/10.1061/(ASCE)0733-9399(1991)117:4(836)

Youssef, N., Nuttall, B., Hata, O., Tahtakran, O., & Hart, G. C. (2000). Building case study: Los Angeles City Hall. *The Structural Design of Tall Buildings*, *9*(1), 3–24. https://doi.org/10.1002/(SICI)1099-1794(200003)9:1%3C3::AID-TAL141%3E3.0.CO;2-R

Zayas, V. A., Low, S. S., & Mahin, S. A. (1990). A simple pendulum technique for achieving seismic isolation. *Earthquake Spectra*, *6*(2), 317–333. https://doi.org/10.1193/1.1585573

Zúñiga-Cuevas, O., & Terán-Gilmore, A. (2012). Control de aceleraciones de entrepiso para sistemas estructurales con aislamiento sísmico de base. *Revista de Ingeniería Sísmica*, *87*, 25–45. https://doi.org/10.18867/ris.87.155

Zúñiga-Cuevas, O., & Terán-Gilmore, A. (2013). Parametric study on acceleration-based design of low-rise base isolated systems. *Engineering Structures*, *53*, 25–37. https://doi.org/10.1016/j.engstruct.2013.03.012